Simulation and Analysis of Ion Detection in DNA Nanopore FET Device

Purun Cao

A thesis

submitted in partial fulfillment of the requirements for

the degree of

Master of Science in Electrical Engineering

University of Washington

2024

Committee:

M. P. Anantram

Lih Y. Lin

Program Authorized to Offer Degree:

Department of Electrical and Computer Engineering

University of Washington

Abstract

Simulation and Analysis of Ion Detection in DNA Nanopore FET Device

Purun Cao

Chair of the Supervisory Committee:
M. P. Anantram
Department of Electrical and Computer Engineering

In this work, a novel ion detection device integrating a DNA-origami nanopore with a field-effect transistor (FET) was designed and modeled to determine the sensitivity of the device within cellular environments. The design employed an "artificial gap junction" constructed using a DNA origami nanopore as a direct interface between the cell and the device. The DNA-origami structure is bio-compatible and can convert signals generated by ionic currents directly into electrical signals by detecting the ions as a buildup of charge. An electrical double layer would form on the nanopore inner wall and over the gate oxide, and the resulting source-drain current can be used to measure the presence of ions in the cell. The electric double layer theory was studied and applied to model ion and potential distributions inside the DNA nanopore. The device combined with the nanopore is shown to have high sensitivity to ion concentration, with the electrical double layer behavior governing the device characteristics. A logarithmic relationship was found between ion concentration and a single FET current, generating up to 200nA of current difference with a small applied bias.

Table of Contents

Chapter 1: Introduction

Overview of Neural-Sensing Based on Semiconductor Technology

The integration of biotechnology with semiconductor nanotechnology marks a significant advance in neuroscience, particularly through the development of devices designed to interface directly with neurons. These innovations provide ways to directly monitor neural signals and thus could facilitate the development of neural science and potentially offer promising new treatments for chronic pain and neurodegenerative diseases like Parkinson's. Using a range of materials from traditional silicon-based microelectrodes to more novel applications like carbon nanotubes [1], researchers aim to develop highly sensitive biosensors capable of monitoring neural activity at high levels of precision.

Although current CMOS devices have length scales comparable to most biological systems, the transmission of biochemical signals from cells to these biosensors involves many challenges, including the biocompatibility of the materials used and the sensitivity required to detect such molecular-level events. Researchers have developed patches equipped with microelectrodes that are positioned near the cell membrane to measure extracellular field potentials and could be used to understand action potential [2]; however, despite the fact that these devices have seen significant improvement with smaller electrode sizes and direct integration into CMOS chips [3], the challenges in biocompatibility and signal sensitivity have not been solved.

Microelectrodes are known to cause reactive tissue responses, namely both acute and chronic inflammations, that would impede the strength of the neuronal signals to be recorded by microelectrodes [1]. Also, their signals tend to be severely attenuated due to the insulating nature of the cellular membrane, decreasing from 10s to 100s of microvolts inside the cell to 10s of millivolts outside the cell even when the electrodes are up against the cellular membrane, significantly reducing the signal-to-noise ratio of these microelectrode sensors [2,4]. As the field continues to evolve, the focus remains on enhancing the biocompatibility and sensitivity of these devices while minimizing their invasiveness. The ultimate goal is to create a seamless interface between electronic biomedical devices and living tissues without interrupting cellular activities, aiming to bridge the gap between biological systems and electronic sensors.

Artificial-Gap-Junction Based on DNA-Origami Nanopore

DNA origami is a nanotechnology technique that uses DNA molecules to create precise, two-dimensional, and three-dimensional shapes at the nanoscale. This method involves folding a long, single-stranded DNA molecule into a desired structure using several short staple strands, which are designed to bind at specific locations along the main strand. The technique enables the creation of complex structures with high precision, which can be used in various applications including drug delivery, biosensing, and building more complex molecular machines.

To solve the previously mentioned challenges, this thesis proposes using DNA origami nanopore as an artificial ion channel to directly guide cellular electrolytes to the semiconductor device to be measured. In this study, we use the dimensions of a DNA origami nanopore constructed in a six-helix bundle topology [5,6], as shown in Figure 1.

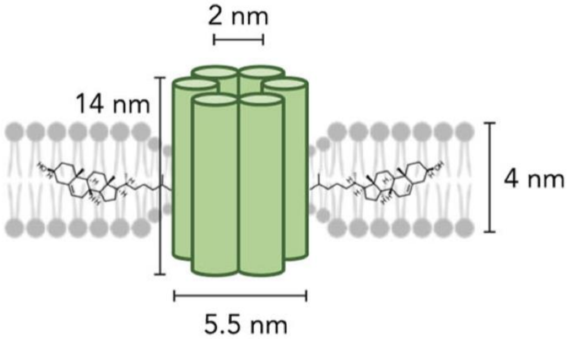

Figure 1. DNA-origami 6-helix bundle nanopore anchored to the lipid bilayer membrane [6].

The DNA-origami nanopore can be modified with ligands to anchor to the lipid bilayer on a cell, as this has already been demonstrated experimentally in a constructed supported bilipid bilayer (SLB) [6]. In sensing the cellular environment, the DNA nanopore could form a stable trans-membrane pore, and its self-assembly properties allow it to be customized, varying pore size or integrating the nanopore into a larger device. This method would not need to penetrate or slice the cellular membrane and would potentially cause minimal disturbance to the tissue. As the semiconductor device would be able to make contact with the cellular electrolyte directly without the insulating membrane, the measured signal should have much more sensitivity to enable molecular-level measurement.

Our research complements current experimental work to design and model an in-vivo device. We have developed a novel approach by combining DNA-origami nanopores with field-effect transistors, or FETs, and our research focuses on the computational analysis of such devices. One end of the DNA-origami nanopore is anchored to the lipid bilayer on a cell, while the other end of the DNA-origami structure is connected to the gate of a nano-transistor, as shown in Figure 2.

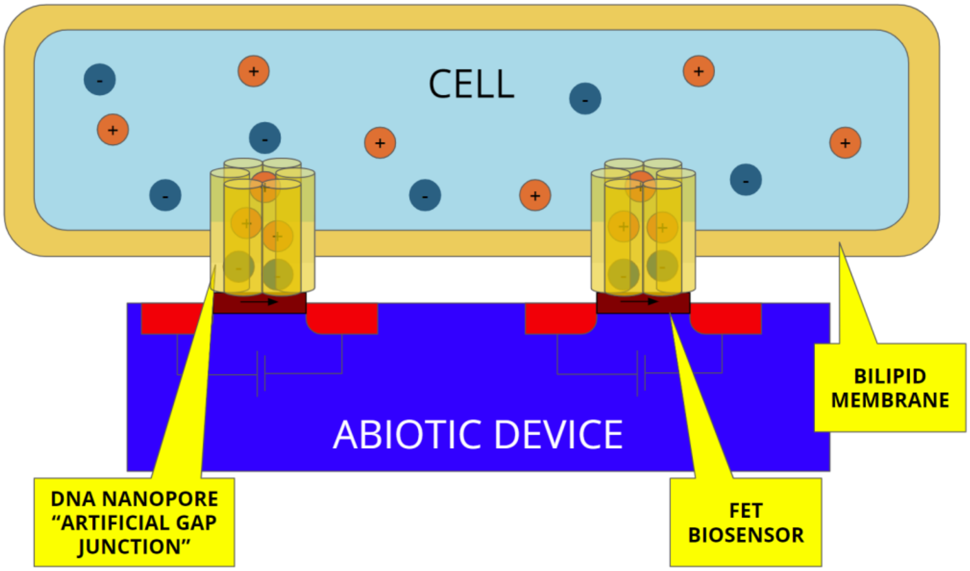

Figure 2. Illustration showing cell connected to the FET device through the DNA-origami nanopore channel that acts as the artificial gap junction. This figure has been reproduced from [7], where it was created by William Livernois and I was a co-author.

While typical nanopore sensors detect single molecules and ions by measuring the change in ion flow across a membrane [8], the proposed device would detect the ions as a buildup of charge across the gate of the FET. A blanket of ions (electrical double layer) would form over the negatively charged nanopore inner wall and the gate oxide, depending on the local environment. This charge buildup would modulate the conductance in the transistor channel, and thus, the resulting source-drain current can be used to measure the presence of ions in the cell.

Chapter 2: First Principles Models in Modeling Electrical Double Layers

As the proposed device's characteristics are primary governed by the electrical double layer in this thesis, it is important to fully understand the physical models describing it. In this chapter, we will examine the formulation and derivation of 3 variations and modifications to the model, as well as establish corresponding numerical 1-dimensional solvers for these variations as a base line for comparison to the 3-dimensional models in later stages.

Electrical Double Layers: A Brief Introduction

In surface science, an electrical double layer (EDL) is a structure that appears on the charged surface of an object when it is exposed to an electrolyte, as shown in Figure 3. The EDL refers to two parallel layers of charge surrounding the object’s charged surface. The first compact layer is at the surface (either positive or negative depending on the object’s surface charge). The second diffuse layer is composed of ions attracted to the surface charge via the Coulomb force, and is made of free ions that move in the fluid under the influence of electric attraction and thermal motion.

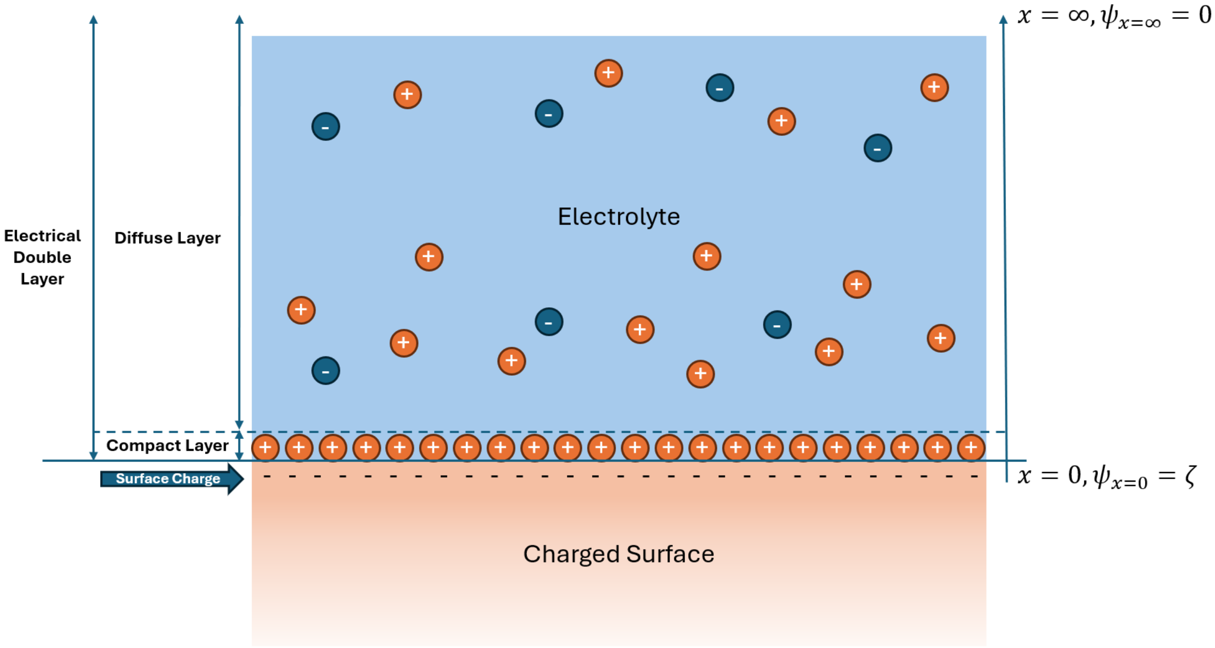

Figure 3. Schematic of the electrical double layer (EDL) in aqueous solution at the interface with a negatively-charged surface.

In our application, we will approximate the solid surface in Figure 3 to be the charged surface of the DNA-origami nanopore with an approximated surface charge density calculated from the density of phosphates facing inward in the six-helix bundle in the DNA nanopore. Based on a base pair spacing of 3.4Å for B-DNA, resulting in an average of 6 phosphates facing the inside of the pore across a 4nm diameter pore, the charge density was calculated to be

$$\sigma = \frac{6 \cdot (-1)q}{\pi \cdot 4\,nm \cdot 3.4\text{Å}} = -1.4 \times 10^{14}\,\frac{q}{cm^2} \qquad (1)$$

where q stands for elemental charge of $1.6 \times 10^{-19}\,C$.

Original Poisson-Boltzmann Equation

The Poisson-Boltzmann equation provides a foundational understanding of the electrical double layer at the interface between a charged surface and an electrolyte solution. Developed independently by Gouy and Chapman in the early 20th century, this model conceptualizes how ions distribute themselves near a charged surface, leading to a diffuse layer of charge that counterbalances the surface charge. The equation describes the distribution of the electric potential in a solution near a charged surface. This distribution is important to determine how the electrostatic interactions will affect the molecules in solution and, in our case, how ions in electrolyte would behave under the influence of the charged DNA-origami nanopore.

The Poisson-Boltzmann equation couples the Poisson's equation for potential ψ and the Boltzmann distribution of ion concentration c_i of the i^{th} ionic species in the electrolyte (in this work, only binary electrolyte is modeled; as a result, only c_p for anions and c_n for cations are considered).

The potential distribution described by the Poisson equation is:

$$\varepsilon_0 \nabla \cdot (\varepsilon_r \nabla \psi) = -q \sum z_i c_i \tag{2}$$

where ε_o is the permittivity of free space, and ε_r is the relative permittivity of solvent.

The transport of the i^{th} ionic species is governed by the Nernst-Planck equation,

$$\frac{dc_i}{dt} + \nabla \cdot J_i = 0 \tag{3}$$

$$J_i = -D_i \nabla c_i - \mu_i c_i \nabla \psi \tag{4}$$

where J_i is the flux density, D_i is the diffusivity, and μ_i is the mobility. The diffusivity and mobility of the electrolyte can be related using the Einstein relation given by

$$\frac{D_i}{\mu_i} = \frac{k_B T}{z_i q} \tag{5}$$

where, k_B is the Boltzmann constant, T is the absolute temperature, q is the elementary charge and z_i is the valence of that ionic species.

In a 1-dimensional wall geometry with the charged surface at $x = 0$ (see Figure 3 for reference), assuming that the concentration is at equilibrium, we can simplify the Nernst-Planck equation to:

$$\frac{d}{dx}\left(-D_i\frac{dc_i}{dx} - \frac{z_i q D_i c_i}{k_B T}\frac{d\psi}{dx}\right) = 0 \tag{6}$$

Integrating equation 6 assuming bulk characteristics at far away, that is, $\left(\frac{d\psi}{dx}\right)_{x=\infty} = 0$ and $\left(\frac{dc_i}{dx}\right)_{x=\infty} = 0$, we get,

$$\frac{z_i q}{k_B T}\frac{d\psi}{dx} + \frac{d(ln\ \ c_i\ )}{dx} = 0 \tag{7}$$

Again, assuming bulk characteristics at far away, $(\psi)_{x=\infty} = 0, (c_i)_{x=\infty} = c_{i0}$ where c_{i0} is the concentration at bulk, integrating equation 7, we get the Boltzmann distribution of ions,

$$c_i = c_{i0}\exp\left(-\frac{z_i q\psi}{k_B T}\right) \tag{8}$$

With a symmetric binary electrolyte, $z_p = -z_n = z$ and $c_{p0} = c_{n0} = c_0$, and coupling with Poisson's equation, we have derived the Poisson-Boltzmann equation:

$$\nabla^2\psi = \frac{2zqc_0}{\varepsilon_r\varepsilon_0} sinh\left(\frac{zq\psi}{k_B T}\right) \tag{9}$$

Given the Poisson-Boltzmann equation, we can also derive the Grahame equation, which calculates the zeta potential (the potential at the surface) from surface charge.

Define a dimensionless potential $y \equiv e^{\frac{zq\psi}{k_B T}}$, and thus the Poisson-Boltzmann equation in 1-dimension could be re-written as:

$$\frac{d^2y}{dx^2} = \frac{2c_0 z^2 q^2}{\varepsilon_r\varepsilon_0 k_B T}\sinh y = \kappa^2 \cdot \sinh y \tag{10}$$

By multiply both sides by $2 \cdot \frac{dy}{dx}$, we have:

$$2 \cdot \frac{dy}{dx} \cdot \frac{d^2y}{dx^2} = 2 \cdot \frac{dy}{dx} \cdot \kappa^2 \cdot sinh\,y \tag{11}$$

Notice the left side is equal to $\frac{d}{dx}\left(\frac{dy}{dx}\right)^2$, we can integrate it to obtain:

$$\int \frac{d}{dx'}\left(\frac{dy}{dx'}\right)^2 dx' = 2\kappa^2 \cdot \int \frac{dy}{dx'} \cdot sinh\, y \cdot dx' \tag{12}$$

$$\left(\frac{dy}{dx}\right)^2 = 2\kappa^2 \cdot (cosh\, y + C_1) \tag{13}$$

At large distances, the dimensionless potential y and its derivative are zero. Since $\cosh y = 1$ for $y = 0$, $C_1 = -2\kappa^2$. Thus, we can derive $\frac{dy}{dx}$ as follows (notice here a negative surface charge (thus, positive $\frac{dy}{dx}$) is assumed.

$$\left(\frac{dy}{dx}\right)^2 = 2\kappa^2 \cdot (cosh\, y - 1) \tag{14}$$

$$\frac{dy}{dx} = -\kappa \cdot \sqrt{2\, cosh\, y - 2} = -2\kappa \cdot sinh \frac{y}{2} \tag{15}$$

Since for electroneutrality, the surface charge density would be the opposite of the integral of charge concentration in the double layer, as labeled in Figure 3:

$$\sigma = -\int_0^\infty q \sum z_i c_i \, dx \tag{16}$$

Using the 1-dimensional Poisson's equation (equation 2) and taking ε_r to be a constant, we have:

$$\sigma = \varepsilon_r \varepsilon_0 \int_0^\infty \frac{d^2\psi}{dx^2} \cdot dx = -\varepsilon_r \varepsilon_0 \left[\frac{d\psi}{dx}\right]_{x=0} \tag{17}$$

Notice that at $x = \infty$, the potential and its gradient are zero. Combining this with the derived $\frac{dy}{dx}$, we have:

$$\frac{dy}{dx} = \frac{d\left(\frac{zq\psi}{k_B T}\right)}{dx} = \frac{zq}{k_B T} \cdot \frac{d\psi}{dx} \tag{18}$$

As we denote zeta potential to be the potential at the surface $\zeta = \psi_{x=0}$ (shown in Figure 3) we have the Grahame equation:

$$\sigma = \sqrt{8\varepsilon_r \varepsilon_0 k_B T} \cdot sinh\left(\frac{zq\psi_{x=0}}{2k_B T}\right) \tag{19}$$

$$\zeta = \frac{2k_B\, T}{zq} sinh^{-1}\left(\frac{\sigma}{\sqrt{8c_0 \varepsilon_r \varepsilon_0 k_B T}}\right) \tag{20}$$

Finite Ion Effect – The Bikerman Model

In the previous section, the Poisson-Boltzmann equation assumed that the ion species in the electrolyte are point charges; however, in reality, ion species are much larger, and their finite size need to be considered. This problem becomes serious in certain situations. For example, the concentration of counter-ions can be unreasonably high near the charged surface if the size of ions are neglected, i.e., in our case, near the charged DNA nanopore.

Among the many modification of Poisson-Boltzmann equation with steric effect included to account for the finite volume of ions, the Bikerman model [9] has been popular due to its ease of application and qualitatively good agreement with experiments [10].

In the Bikerman model, ion species and the solvent molecules are treated as hard spheres and assumed to have the same diameter a. Assuming a binary electrolyte, the free energy is given as:

$$F = U - TS \tag{21}$$

$$U = \int \left[-\frac{\varepsilon}{2} |\nabla\psi|^2 + z_p q \psi c_p + z_n q \psi c_n \right] dV \tag{22}$$

$$-TS = \int k_B T \left[c_p \, log(c_p a^3) + c_n \, log(c_n a^3) + \frac{(1 - c_p a^3 - c_n a^3)}{a^3} log(1 - c_p a^3 - c_n a^3) \right] dV \tag{23}$$

where U is the internal energy, S is the entropy, and T is the temperature.

By taking the derivative of F with respect to c_p and c_n, we have the chemical potential of cation and anion μ_p and μ_n (This is the definition of chemical potential).

$$\frac{\delta F}{\delta c_p} = \mu_p = z_p q \psi + k_B T [log(c_p a^3) - log(1 - c_p a^3 - c_n a^3)] \tag{24}$$

$$\frac{\delta F}{\delta c_n} = \mu_n = z_n q \psi + k_B T [log(c_n a^3) - log(1 - c_p a^3 - c_n a^3)] \tag{25}$$

We can rewrite the chemical potentials (equation 24 and 25) as:

$$\frac{c_p a^3}{1 - c_p a^3 - c_n a^3} = e^{\frac{\mu_p - z_p q \psi}{k_B T}} \tag{26}$$

$$\frac{c_n a^3}{1 - c_p a^3 - c_n a^3} = e^{\frac{\mu_n - z_n q \psi}{k_B T}} \tag{27}$$

Using equation 26 and 27, we can derive:

$$\frac{c_p}{c_n} = e^{\frac{(\mu_p - \mu_n) - (z_p - z_n) q \psi}{k_B T}} \tag{28}$$

Since at equilibrium, the chemical potential of any given species must be the same throughout the system, the chemical potential everywhere should be equal to the chemical potential at bulk ($\mu_n = \mu_{n0}, \mu_p = \mu_{p0}$). As at bulk, conditions are $c_p = c_{p0}$, $c_n = c_{n0}$, $c_p z_p + c_n z_n = 0$ and $\psi = 0$, we have:

$$c_p = -c_n \frac{z_n}{z_p} e^{-\frac{(z_p - z_n) q \psi}{k_B T}} \tag{29}$$

Substituting equation 29 back into equation 27, we have:

$$c_n = \frac{1}{a^3} \frac{1}{1 + e^{-\frac{\mu_n - z_n q \psi}{k_B T}} - \frac{z_n}{z_p} e^{-\frac{(z_p - z_n) q \psi}{k_B T}}} \tag{30}$$

Again, using uniform chemical potential, assuming bulk condition, $c_p = c_{p0}$, $c_n = c_{n0}$, $c_p z_p + c_n z_n = 0$ and $\psi = 0$, we can derive from equation 30:

$$e^{\frac{\mu_n}{k_B T}} = \frac{c_{n0} a^3}{1 - (c_{p0} + c_{n0}) c_{n0} a^3} \tag{31}$$

Substituting equation 31 back into equation 30, we now have the anion concentration:

$$c_n = \frac{c_{n0} e^{-\frac{z_n q \psi}{k_B T}}}{1 - (c_{p0} + c_{n0}) a^3 + (c_{p0} + c_{n0}) a^3 \frac{z_p e^{-\frac{z_n q \psi}{k_B T}} - z_n e^{-\frac{z_p q \psi}{k_B T}}}{z_p - z_n}} \tag{32}$$

Substituting equation 32 back into equation 29, we have the cation concentration:

$$c_p = \frac{c_{p0} e^{-\frac{z_p q \psi}{k_B T}}}{1 - \left(c_{p0} + c_{n0}\right) a^3 + \left(c_{p0} + c_{n0}\right) a^3 \frac{z_p e^{-\frac{z_n q \psi}{k_B T}} - z_n e^{-\frac{z_p q \psi}{k_B T}}}{z_p - z_n}} \tag{33}$$

Simplify to $z_p = -z_n = z$ and $c_{p0} = c_{n0} = c_0$ for symmetric binary electrolyte, we have:

$$c_p = \frac{c_0 e^{-\frac{zq\psi}{k_B T}}}{1 - 2c_0 a^3 + 2c_0 a^3 \cosh\left(\frac{zq\psi}{k_B T}\right)} \tag{34}$$

$$c_n = \frac{c_0 e^{\frac{zq\psi}{k_B T}}}{1 - 2c_0 a^3 + 2c_0 a^3 \cosh\left(\frac{zq\psi}{k_B T}\right)} \tag{35}$$

Thus, with modified cation and anion concentration replacing Boltzmann distribution, coupling with Poisson's equation (equation 2), the modified Poisson-Boltzmann equation now is:

$$\nabla^2 \psi = \frac{2zqc_0}{\varepsilon_r \varepsilon_0} \frac{sinh\left(\frac{zq\psi}{k_B T}\right)}{1 - 2c_0 a^3 + 2c_0 a^3 cosh\left(\frac{zq\psi}{k_B T}\right)} \tag{36}$$

Electric Field Dependence of Permittivity of Polar Dielectrics

In the previous sections, we described the electrical double layer considering the solvent as a dielectric medium of constant permittivity. This assumption allowed us to neglect the interaction between solvent molecules and the electric field. However, since the water molecule is considered a polar dielectric, the relative permittivity of an electrolyte solution near the highly charged surface may be substantially decreased due to the orientational ordering of water dipoles.

In a polar dielectric, as the electric field increases, a point of saturation will eventually be reached where nearly all the dipoles are aligned with the field. Beyond this saturation point, the alignment of additional dipoles is minimal because they are already oriented in the direction of the field. Once the dipoles are fully aligned, further increases in the electric field cannot enhance their alignment. This results in a decrease in the material's polarizability, leading to a reduction in permittivity.

Such relationship could be described via the Booth’s field-dependent permittivity model [11],

$$\varepsilon_r = n^2 + [\varepsilon_r^0 - n^2]\left[\frac{3}{\beta\left|-\frac{d\psi}{dx}\right|}\right]\left[coth\left(\beta\left|-\frac{d\psi}{dx}\right|\right) - \frac{1}{\beta\left|-\frac{d\psi}{dx}\right|}\right] \qquad (37)$$

$$\beta = \frac{5\mu^p}{2kT}(n^2+2)$$

where, ε_r is the relative permittivity of the solvent, n is the refractive index of the solvent, ε_r^0 is the field-independent relative permittivity of the solvent and μ^p is the dipole moment of the solvent.

In our case, as the polar solvent we considered is water, using this model, we can see that under high electric field near the DNA charged surface as shown in Figure 4, the relative permittivity has a significant change, reduced by more than 50%.

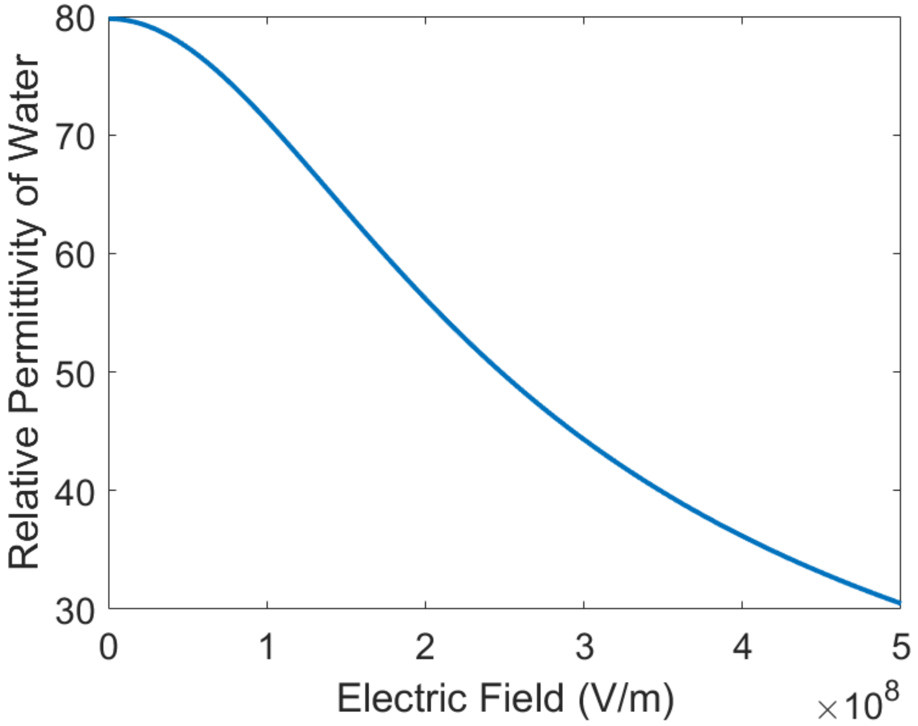

Figure 4. The relationship between electric field and relative permittivity of water calculated from Booth's model.

This electric field dependent permittivity could be easily incorporated into either the original Poisson-Boltzmann equation or the finite-ion modification by replacing the constant relative permittivity term.

Methodology and Implementation of 1D Infinite Slab Solver

With the original Poisson-Boltzmann equation (equation 8) and two of its modifications established, 1D solvers for an infinite slab geometry as shown in Figure 3 were made to further understand how cellular electrolyte near charged surfaces similar to that of the DNA-nanopore would behave, and, subsequently, serves as a reference point for more complex geometries.

All models and modifications mentioned are nonlinear differential equations in nature. Such nonlinear system is approached using Newton's method. This involves discretizing a nonlinear ODE or PDE into a system of equations, leading to a series of nonlinear equations.

A nonlinear system of equations $F(\psi) = 0$ is obtained if we discretize a nonlinear ODE or PDE into $n + 1$ points spanning the solution interval and m equations, i.e.,

$$\begin{cases} F_1(\psi_0, \psi_1, \psi_2, \psi_3, \dots, \psi_n) = 0 \\ \dots \\ F_m(\psi_0, \psi_1, \psi_2, \psi_3, \dots, \psi_n) = 0 \end{cases} \tag{38}$$

In the original Poisson-Boltzmann equation case, we could discretize and estimate $F(\psi) = \nabla^2\psi - \frac{2zqc_b}{\varepsilon_r\varepsilon_0} sinh\left(\frac{zq\psi}{k_BT}\right)$ as: $F_i(\psi_0, \psi_1, \psi_2, \psi_3, \dots, \psi_n) = \frac{\psi_{i-1} - 2\psi_i + \psi_{i+1}}{h^2} - \frac{2zqc_b}{\varepsilon_r\varepsilon_0} sinh\left(\frac{zq\psi_i}{k_BT}\right)$, $i = 1,2,3, \dots, n-1$, and h represents grid space.

Similarly, in the finite ion size case, we could discretize and estimate $\mathrm{F}(\psi) = \nabla^2\psi - \frac{2zqc_0}{\varepsilon_r\varepsilon_0} \frac{sinh\left(\frac{zq\psi}{k_BT}\right)}{1 - 2c_0a^3 + 2c_0a^3 cosh\left(\frac{zq\psi}{k_BT}\right)}$ as: $F_i(\psi_0, \psi_1, \psi_2, \psi_3, \dots, \psi_n) = \frac{\psi_{i-1} + 2\psi_i + \psi_{i+1}}{h^2} - \frac{2zqc_0}{\varepsilon_r\varepsilon_0} \frac{sinh(\frac{zq\psi_i}{k_BT})}{1 - 2c_0a^3 + 2c_0a^3 cosh(\frac{zq\psi_i}{k_BT})}$.

In electric field dependent permittivity case, as now ε_r depend on x as well, $F(\psi)$ now becomes $F(\psi) = \nabla \cdot (\varepsilon_r \nabla\psi) - \frac{2zqc_b}{\varepsilon_0} sinh\left(\frac{zq\psi}{k_BT}\right)$ and we can discretize and estimate it as: $F_i(\psi_0, \psi_1, \psi_2, \psi_3, \dots, \psi_n) = \frac{\psi_{i-1} - 2\psi_i + \psi_{i+1}}{h^2} \varepsilon_{ri} + \frac{\varepsilon_{ri+1} - \varepsilon_{ri}}{h} \frac{\psi_{i+1} - \psi_i}{h} - \frac{2zqc_b}{\varepsilon_0} sinh\left(\frac{zq\psi_i}{k_BT}\right)$. Note that although a new variable ε_{ri} is added to represents the relative permittivity at each point, they could still be calculated from ψ_i through the electric field dependence of permittivity established in equation 37.

The system of nonlinear equations can generally be solved by Newton's method. Given an initial guess $\psi^{(0)}$, the Newton iteration is:

$$\psi^{(k+1)} = \psi^{(k)} - (J(\psi^{(k)})^{-1} F(\psi^{(k)})) \tag{39}$$

where k is the iteration number and $J(\psi)$ is the Jacobian matrix defined as

$$J(\psi) = \begin{bmatrix} \frac{\partial F_1}{\partial \psi_1} & \cdots & \frac{\partial F_1}{\partial \psi_{n-1}} \\ \vdots & \ddots & \vdots \\ \frac{\partial F_m}{\partial \psi_1} & \cdots & \frac{\partial F_m}{\partial \psi_{n-1}} \end{bmatrix} \tag{40}$$

With a boundary condition $\psi(x = 0) = -0.11V$, which is calculated from DNA surface charge in equation 1 using equation 20

$$\zeta = \frac{2k_B T}{zq} sinh^{-1}\left(\frac{\sigma}{\sqrt{8c_0\varepsilon_r\varepsilon_0 k_B T}}\right) \tag{20}$$

for 1D wall geometry with a symmetric binary electrolyte with a concentration of 0.2M and $z_p = -z_n = 1$, the numerical solution of original Poisson-Boltzmann equation matches the analytical solution [12], thus verifying the numerical method used, as shown in Figure 5.

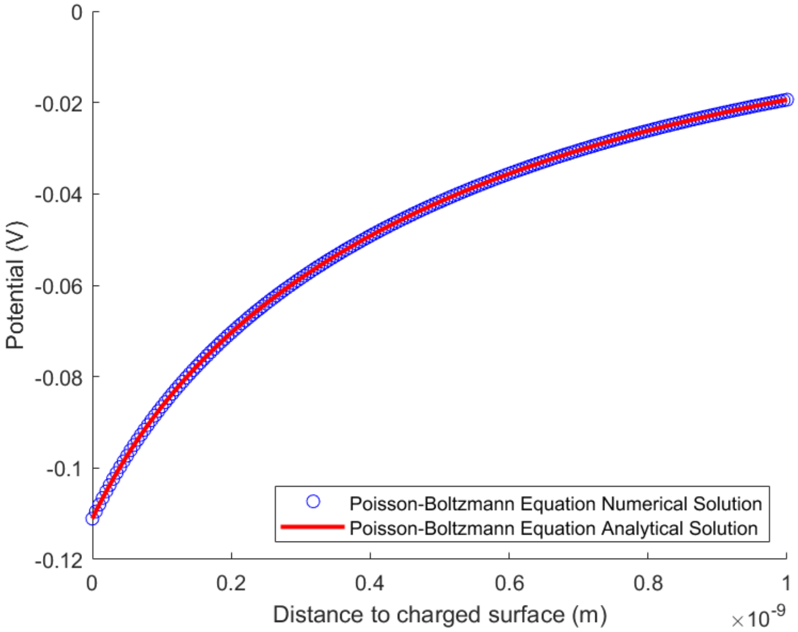

Figure 5. Relationship between distance to charged surface and potential of the electrical double layer in nanopore-electrolyte setting. Comparison of Analytical and Numerical Solution of the Original Poisson-Boltzmann equation.

Under the same geometry and conditions and assuming an ionic diameter of 0.5 nm, the two modifications of the Poisson-Boltzmann equation are also calcuated, and we also combine the two modifications and designate the combined model as the modified Poisson-Boltzmann equation. Thus, we have four models in total in comparison: the original Poisson-Boltzmann, the finite ion size modification, the electric field dependent permitivity modification, and the modified Poisson-Boltzmann combining the two modifications. Results from all four models are compared as shown in Figure 6.

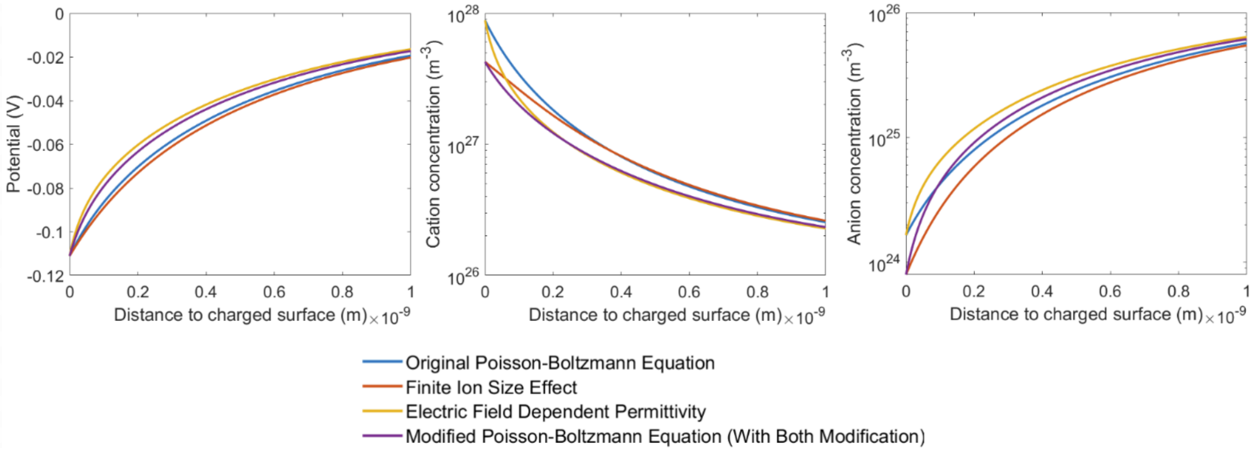

Figure 6. Comparison of All Models. Relationship between distance to charged surface and potential, cation concentration, anion concentration of the electrical double layer in nanopore-electrolyte setting.

Chapter 3: Understanding the surface charge of the SiO2 gate

With the mechanism of the electrical double layer established, now we can freely calculate the potential and charge distribution in binary electrolyte near surfaces with different surface charges. Although we already have an estimation of DNA-nanopore's surface charge, in our proposed device, however, it would not be the only charged surface in the system. In reality, the gate of the nano-transistor (silicon oxide, SiO_2) in contact with electrolyte would also be charged.

Site-binding Model

The mechanism responsible for the silicon oxide surface charge can be described by the site binding model [13], which describes the equilibrium between the $SiOH$ surface sites and the H^+ ions in the solution. The reactions are:

$$SiO^- + H^+ \leftrightarrow SiOH$$
$$SiOH + H^+ \leftrightarrow SiOH_2^+$$

From these reactions, we thus have this set of thermodynamics equations:

$$\mu_{SiOH} = \bar{\mu}_{SiO^-} + \bar{\mu}_{H^+} \quad (41)$$

$$\bar{\mu}_{SiOH_2^+} = \mu_{SiOH} + \bar{\mu}_{H^+} \quad (42)$$

where μ represents chemical potential and $\bar{\mu}$ represents electrochemical potential.

The electrochemical potentials can be written as:

$$\bar{\mu}_{H^+} = \mu_{H^+} + q\psi_B \quad (43)$$

$$\bar{\mu}_{SiOH_2^+} = \mu_{SiOH_2^+} + q\psi_S \quad (44)$$

$$\bar{\mu}_{SiO^-} = \mu_{SiO^-} - q\psi_S \quad (45)$$

where ψ_B is the electric potentials in the bulk of the solution, and ψ_S is the electric potentials at the oxide surface.

Given that:

$$\mu_x = \mu_x{}^0 + kTln(a_x) \quad (46)$$

where $\mu_x{}^0$ is the standard chemical potential of species x, and a_x is either the dimensionless activity of the bulk protons H^+ or the number of sites in moles per unit area ν of one of the surface groups. In combination with electrochemical potentials (equation 43 to 45) and substituting the result in the thermodynamics equations (equation 41 and 42), we have:

$$\mu^0_{SiOH} + kT\,ln\,v_{SiOH} = \mu^0_{SiO^-} + kT\,ln\,v_{SiO^-} - q\psi_S + \mu^0_{H^+} + kT\,ln\,a_{H^+} + q\psi_B \quad (47)$$

$$\mu^0_{SiOH_2^+} + kT\,ln\,v_{SiOH_2^+} = \mu^0_{SiOH} + kT\,ln\,v_{SiOH} + \mu^0_{H^+} + kT\,ln\,a_{H^+} + q\psi_B \quad (48)$$

With $\psi_0 = \psi_S - \psi_B$ and the Boltzmann equation, the activity of the bulk protons a_{H^+} can be related to the activity of the protons in the direct vicinity of the oxide surface, $a_{H_S^+}$:

$$a_{H_S^+} = a_{H^+}e^{-\frac{q\psi_0}{kT}} \quad (49)$$

With the dimensionless intrinsic dissociation constants:

$$K_a = exp\left(\frac{\mu^0_{SiOH} - \mu^0_{SiO^-} - \mu^0_{H^+}}{kT}\right) \tag{50}$$

$$K_b = exp\left(\frac{\mu^0_{SiOH_2^+} - \mu^0_{SiOH} - \mu^0_{H^+}}{kT}\right) \tag{51}$$

Thus, we can rewrite the thermodynamics equations as:

$$\frac{v_{SiO^-} \cdot a_{H_S^+}}{v_{SiOH}} = K_a \tag{52}$$

$$\frac{v_{SiOH} \cdot a_{H_S^+}}{v_{SiOH_2^+}} = K_b \tag{53}$$

On the oxide surface, the possible surface sites could either be $\mathrm{SiO^-}$, SiOH, and $\mathrm{SiOH_2^+}$, as shown in Figure 7 below.

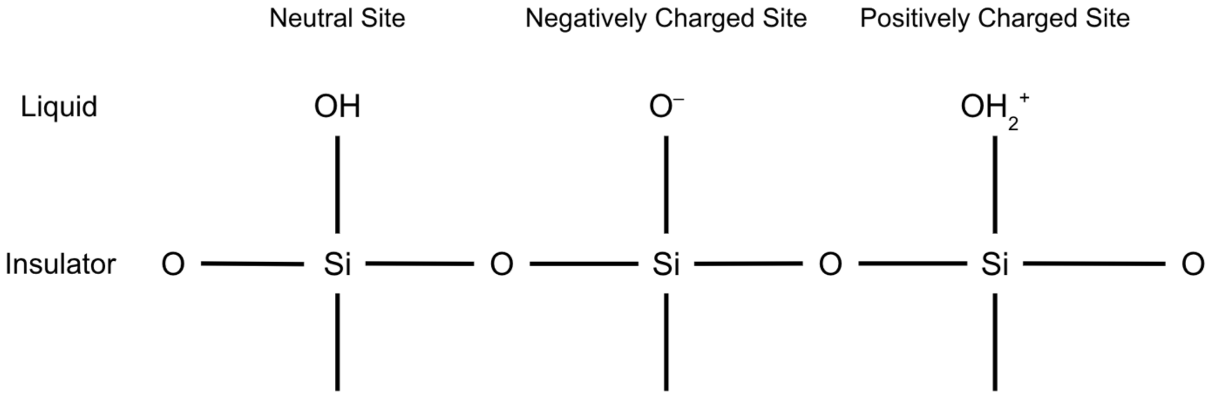

Figure 7. Possible surface sites of SiO2 in water.

Thus, the number of surface sites per unit area, N_s can be represented as:

$$N_s = v_{SiOH} + v_{SiO^-} + v_{SiOH_2^+} \tag{54}$$

Thus, combining with the thermodynamics equations, the surface charge concentration could be written as:

$$\sigma_S = q\left(v_{SiOH_2^+} - v_{SiO^-}\right) = qN_S\left[\frac{a_{H_S^+}^2 - K_aK_b}{a_{H_S^+}^2 - K_b a_{H_S^+} + K_aK_b}\right] \tag{55}$$

$$a_{H_S^+} = a_{H^+} e^{-\frac{q\psi_0}{kT}}$$

This equation calculates the surface charge concentration σ_S using the surface potential ψ_0. Conveniently, we could solve the equation self-consistently along with the Grahame equation (equation 20), which calculates back the surface potential ψ_0 using the surface charge concentration σ_S.

pH Dependence of SiO2 Surface Charge

Back to our case, for the charge of a silicon oxide-water interface in our device, we could use the previously described site-binding model to solve for surface charge. The variable $a_{H^+_{\square}}$ could be assumed to be the concentration of hydrogen in the bulk electrolyte, which is given by the $10^{-pH}\ M$ of the bulk electrolyte, and $a_{H_S^+}$ could be calculated from $a_{H^+_{\square}}$ as mentioned above.

Numerical self-consistent solver coupling Grahame equation (equation 20) and equation 55 was implemented for solving the surface charge concentration on the SiO2 surface. The surface potential, or zeta potential ($\psi_0 = \zeta$ in the equation above) was first guessed to be 0 V, and an initial surface charge was calculated using equation 55. Then, the surface charge is used to re-calculate the zeta potential using Grahame equation. The process is repeated until a stable solution is found.

Assuming the electrolyte to be 0.2M NaCl at neutral pH, and taking the values of N_S, K_a, and K_b be $5 \times 10^{14} cm^{-2}$, $10^{-6}\ M$, and $10^{2}\ M$ respectively [14], a surface charge density $\sigma_s = -1.01 \times 10^{14} \frac{q}{cm^2}$ was calculated self-consistently with equation 55 and Grahame equation (equation 20) as mentioned above, and would later be used as the fixed charge at the gate-electrolyte interface in the TCAD simulations.

The pH's influence on the SiO2 surface charge is also studied using the numerical solver with the same 0.2M NaCl electrolyte. The surface charge mostly changes between $\sigma_s = 0$ to $\sigma_s = -5 \times 10^{14} \frac{q}{cm^2}$ from pH of 4 to 10, and with higher pH, the surface charge becomes significantly more negative, as shown in Figure 8 below.

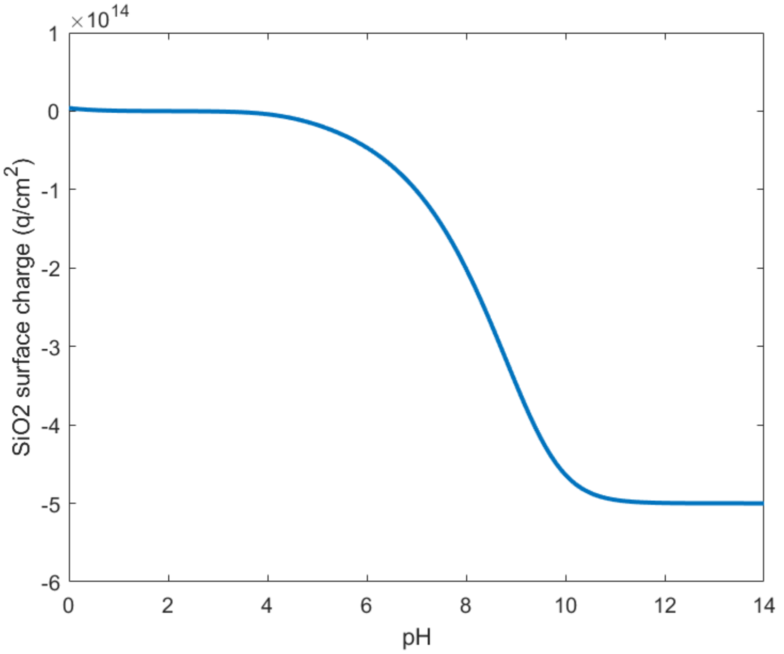

Figure 8. The relationship of SiO2 surface charge concentration and the pH of the electrolyte (0.2M NaCl).

Chapter 4: Model Electrolyte Using Drift Diffusion Through TCAD

Drift Diffusion Model and TCAD

The Drift Diffusion model forms the cornerstone of semiconductor device modeling, capturing the essence of charge carrier transport within these materials. It combines the effects of drift, driven by electric fields, and diffusion, a consequence of concentration gradients, to describe the movement of electrons and holes in semiconductor devices.

The complete drift-diffusion model for semiconductors is based on the following set of equations:

Poisson’s equation is as follows:

$$\nabla^2 V = -\frac{\rho(\boldsymbol{r})}{\varepsilon} \tag{56}$$

where V is the electric potential, ε is the permittivity, and $\rho(\boldsymbol{r})$ is the charge density.

The charge density is given by:

$$\rho(\boldsymbol{r}) = q(N_d^+ - N_a^- + p - n) \tag{57}$$

where N_d^+ and N_a^- are the ionized donor and acceptor concentration, and p and n are hole and electron concentration.

Continuity equation for electron and holes are given by:

$$\frac{\partial n(\boldsymbol{r},t)}{\partial t} = \frac{1}{q}\nabla\cdot\boldsymbol{J_n}(\boldsymbol{r},t) + G_n(\boldsymbol{r},t) - R_n(\boldsymbol{r},t) \tag{58}$$

$$\frac{\partial p(\boldsymbol{r},t)}{\partial t} = -\frac{1}{q}\nabla\cdot\boldsymbol{J_p}(\boldsymbol{r},t) + G_p(\boldsymbol{r},t) - R_p(\boldsymbol{r},t) \tag{59}$$

where J is the electric current density, G is the rate of generation per unit volume per time, potential, and R is the rate of recombination per unit volume per time.

Electric current densities of the electrons and holes are given by:

$$\boldsymbol{J_n}(\boldsymbol{r}) = \boldsymbol{J_n^{(drift)}}(\boldsymbol{r}) + \boldsymbol{J_n^{(diffusion)}}(\boldsymbol{r}) = q\mu_n n\boldsymbol{E} + qD_n\nabla n \tag{60}$$

$$\boldsymbol{J_p}(\boldsymbol{r}) = \boldsymbol{J_p^{(drift)}}(\boldsymbol{r}) + \boldsymbol{J_p^{(diffusion)}}(\boldsymbol{r}) = q\mu_p p\boldsymbol{E} - qD_p\nabla p \tag{61}$$

In the context of Technology Computer-Aided Design (TCAD), solving these equations is pivotal for predicting device behavior under various operating conditions. TCAD tools typically employ numerical methods, such as finite difference, finite element, or Monte Carlo simulations, to solve the Drift Diffusion Equations to better understand device characteristics and performance and enable engineers to optimize semiconductor device design and performance before actual fabrication, significantly reducing development costs and time-to-market. The accuracy and computational efficiency of these methods are continuously improved to address the increasing complexity of modern semiconductor devices, making the Drift Diffusion Equation an indispensable tool in the semiconductor industry.

Using Drift Diffusion to Calculate EDL in TCAD

The Drift Diffusion model is very similar to the Nernst–Planck equation mentioned in chapter 2. When removing generation and recombination and ionized dopant atoms from the drift diffusion equations as they do not exist in electrolytes, the model would give us identical results for the original Poisson-Boltzmann equation.

As a result, in an effort to expand our capabilities to solve more complex 3D geometries for the DNA-origami nanopore sensing device and further other EDL based devices, we modified semiconductor materials in TCAD to exploit such similarity between the equations describing positive and negative ions in the electrolyte and those for holes and electrons in a semiconductor.

In this respect, a symmetric binary electrolyte with valance of 1 can be described as a semiconductor with zero band gap, a constant permittivity, adjusted electron and hole mobility based on corresponding ion mobilities, and an effective density of states in conduction and valence band:

$$N_c = N_v = N_A c_0 \times 10^{-3} \tag{62}$$

where N_A is Avogadro's number and c_0 is the ion molar concentration (M = mol/L) in the bulk of the electrolyte [15].

In Sentaurus TCAD, we were able to convert Silicon to a 0.2M $NaCl$ electrolyte material with relative permittivity of 79.8 and modified electron and hole mobility of $7.591 \cdot 10^{-4}\,\frac{\text{cm}^2}{\text{V}\cdot\text{s}}$ and $5.023 \cdot 10^{-4}\,\frac{\text{cm}^2}{\text{V}\cdot\text{s}}$ based on Cl^- and Na^+ ion mobilities.

To verify such method, both 2D and 3D TCAD slab models are built, as shown in Figure 9, to compare with the previously established 1D numerical solvers in chapter 2. The electrolyte was set to be the previously mentioned 0.2M NaCl, and the dimensions of the electrolyte reservoir in the 2D slab were 20×50 nm and in the 3D slab were 20 (height)×50×50 nm, each with a grounded silicon oxide 2 nm thick electrode (dark red in Figure 9). The interface of the SiO2 electrode and electrolyte was given a charge concentration of $\sigma = -1.4 \times 10^{14}\,\frac{q}{cm^2}$, the same surface charge concentration calculated for the DNA nanopore.

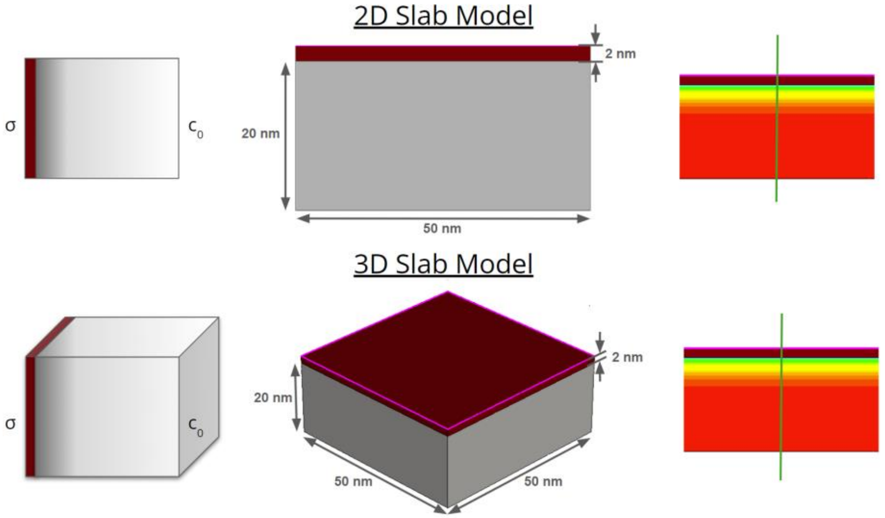

Figure 9. Diagrams of 2D and 3D TCAD slab models showing first the boundary conditions (left) followed by the actual TCAD geometry used for comparison (middle) and the electric potential heatmaps from the TCAD model (right).

Both TCAD models gives us a similar potential along the green cutline shown in Figure 9. When compared to the 1D numerical solvers, the TCAD model matches the original Poisson-Boltzmann equation as expected, and only have a small difference compared to the modified Poisson-Boltzmann equation, as shown in Figure 10. We deem this method to calculate EDL using TCAD as a reasonable approximation and would proceed to model entire EDL-based device in TCAD. Note that the TCAD model does not account for the change in dielectric constant.

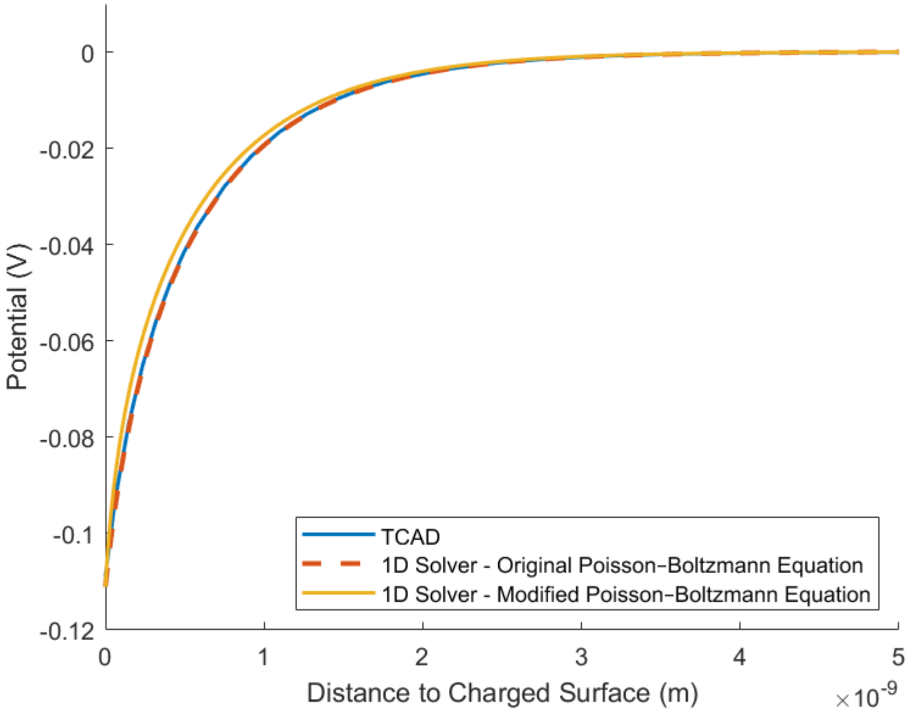

Figure 10. Relationship between distance to charged surface and potential of the electrical double layer, comparison of TCAD slab model and 1D numerical EDL solvers. The first 5 nm from the charged surface is shown.

Chapter 5: Exploratory Device Scale TCAD Simulation

As we have verified that we can model the electrical double layer using TCAD in the previous chapter, in this chapter, we move forward to full sensor device simulation in TCAD.

As an initial exploratory study, a simplified model was used first. For this study, the ions were modeled as a layer of localized charge under a cylindrical dielectric, on top of the gate oxide. Thus, we did not consider the surface charge of the DNA nanopore and instead focused on the geometry of the nanopore and FET device and the effects on overall electrical field on the gate. For this reason, counter ions were not included in these simulations with the assumption that they are not nearby and therefore don't have a significant effect on the gating. The conduction band energy along the channel of the device was obtained across a range of number of ions in the nanopore to demonstrate the sensitivity of such a device.

This setup is depicted in Figure 11, with the ion charge added directly to the interface between the water and the FET without modeling the electrical double layer. Instead, the electrolyte in and above the nanopore was modeled as an insulator with a dielectric constant of 78. Additionally, the relative dielectric constant of the bilipid membrane (in green, surrounding the nanopore) is taken to be 3 based on experimental results [16].

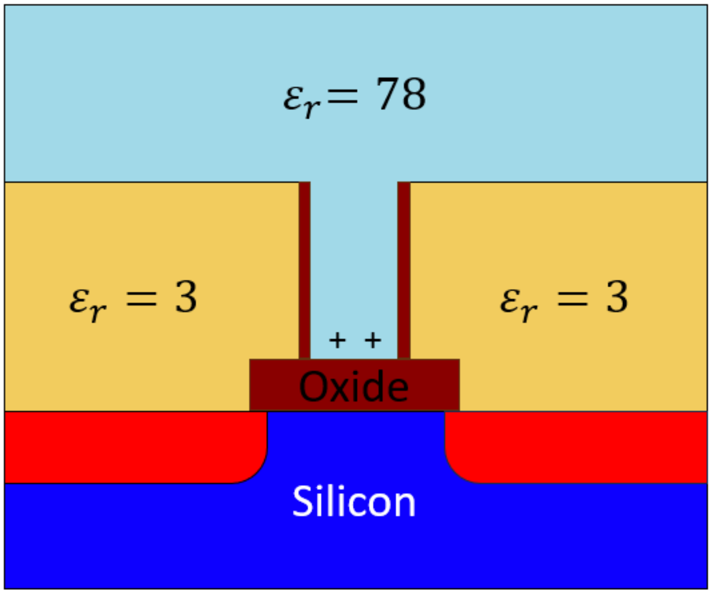

Figure 11. Illustration of the simplified exploratory device, modeling the electrolyte as an insulator with ions only at the interface.

Using this approach allowed us to first look at the feasibility of integration with existing CMOS technology and check underlying assumptions before assessing the electrical characteristics of the full artificial gap junction device.

Initial 2D Exploratory Device Simulation

For simplicity, a 2D approximation of the device was first modeled, as shown in Figure 12. The light blue region on the top represents electrolyte modeled as insulator, the dark red region represents SiO2, the light yellow region represents the bilipid membrane, and the lower section represents silicon (red being n-doped, blue being p-doped). The thickness (into the page) of the 2D model is set to be 4 nm to match the approximate diameter of the DNA-nanopore (2D simulations in Sentaurus requires the length perpendicular to the 2D device structure to be defined.). The charge at the bottom of the nanopore was set to be 0, 1, 2, and 4 cations. The dimensions and doping concentrations were determined relative to values scaled from previously modeled systems [17].

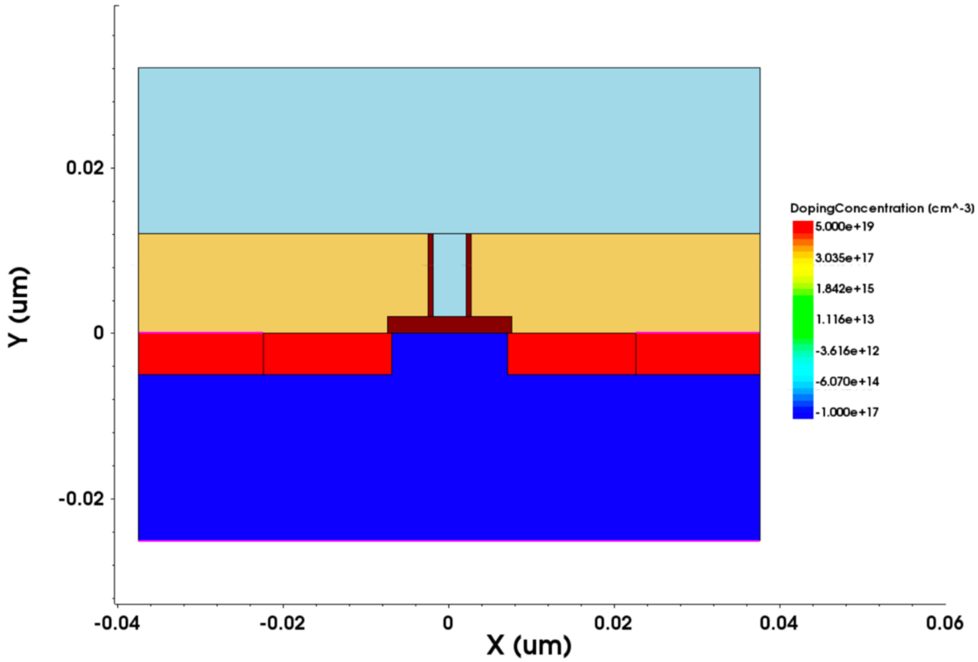

Figure 12. 2D Exploratory Device Structure with abrupt doping changes.

When examining the conduction band energy at zero source drain bias along the channel and 0.1nm below the gate oxide-silicon interface, we observed the conduction band dipping in the middle of the channel caused by the cations placed at the bottom of the nanopore. However, there was an asymmetry in the conduction band accompanied by jumps in the numerical solution, as shown in Figure 13 below.

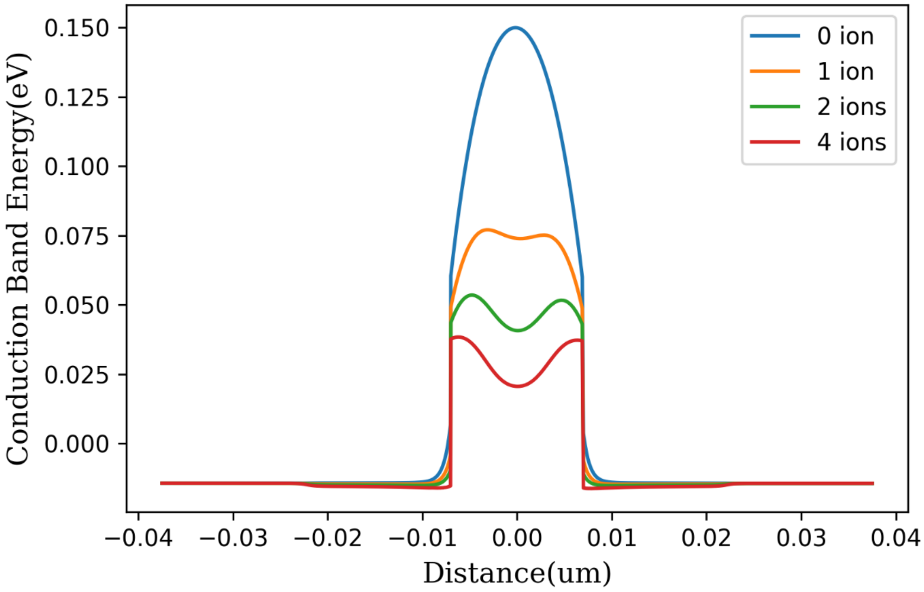

Figure 13. Conduction band energy at zero source drain bias along the channel in 2D exploratory device with abrupt doping changes.

Specifically, at around $x = -0.0075\ \mu m$ and $x = 0.0075\ \mu m$, we can clearly see there is a big abrupt jump in the conduction band for the four cases considered. Further the conduction band is not completely symmetrical, while the device is completely symmetrical under zero source drain bias. We deem this degree of numerical error unacceptable, and upon further examination, we realized that $x = -0.0075\ \mu m$ and $x = 0.0075\ \mu m$ is where the doping concentration abruptly changes from n-type source/drain to p-type channel, and as a result, we suspected that defining such abrupt doping changes along the channel direction cause issues in the numerical solver.

Gaussian Doping Profile for Resolving Numerical Errors

To fix the numerical error mentioned above, a Gaussian profile was used for the n-type doping in the source and drain with a peak value of $5 \cdot 10^{19} cm^{-3}$ in our FET devices. In addition to the n-type doping profile, there is a uniform p-type doping of $1 \cdot 10^{17} cm^{-3}$ in the semiconductor, as shown in Figure 14 below. The idea is to use Gaussian doping profile's gradual change of doping concentration to eliminate the possible numerical difficulties.

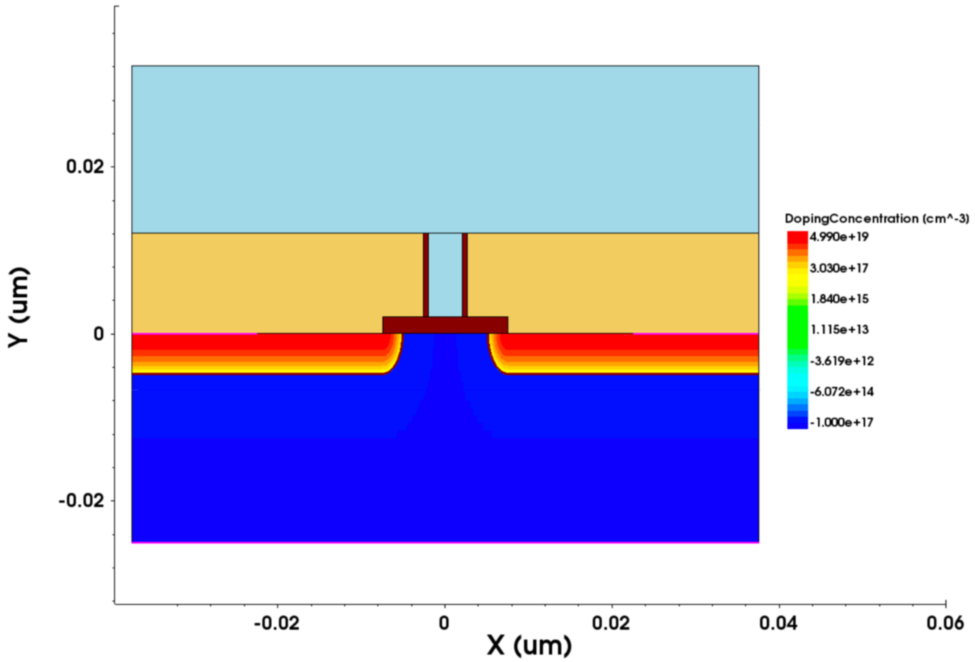

Figure 14. 2D Exploratory Device Structure with Gaussian doping on source and drain.

Figure 15 below shows a close-up of the total doping profile near the source area.

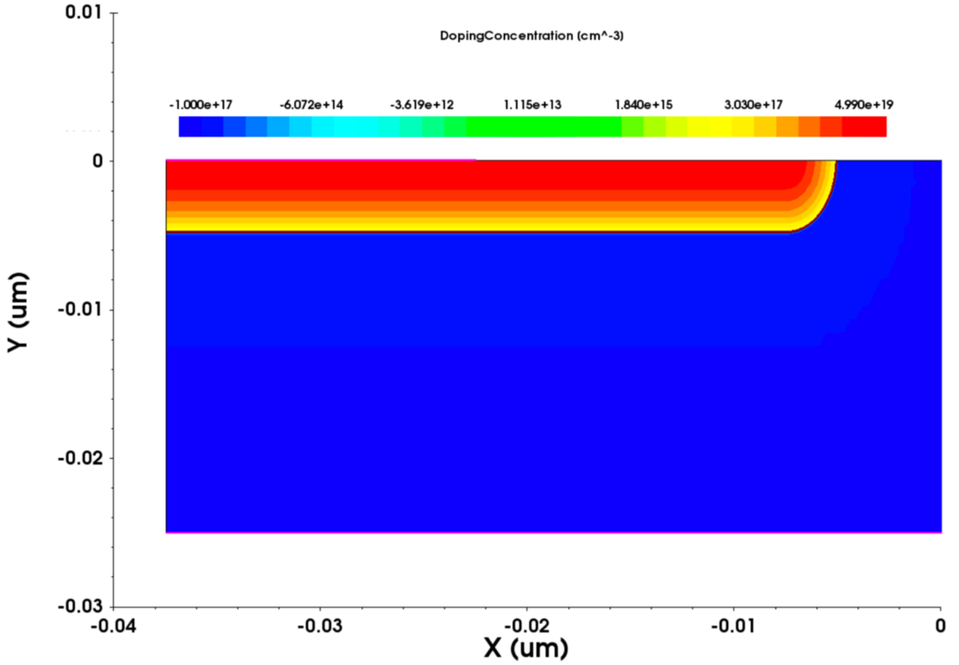

Figure 15. Diagrams of the total doping profiles used in all FET devices modeled.

The doping profile at the source-end is defined by:

$$C(y) = C_{peak} \cdot exp\left(-\frac{\left(y - y_{peak}\right)^2}{2 \cdot \left(stdDev_y\right)^2}\right) for - 0.375\ \mu m < x < -0.0075\ \mu m \tag{63}$$

$$C(x, y) = C(y) \cdot e^{-\frac{(x_0 - x)^2}{2 \cdot (stdDev_x)^2}} for - 0.0075 \mu m < x < 0 \mu m \tag{64}$$

where C_{peak} is the peak n-type doping concentration, y_{peak} is the y-location with this concentration, and

$$stdDev_y = \frac{\text{depth} - y_{\text{peak}}}{\sqrt{2} \cdot \ln\left(\frac{C_{\text{at depth}}}{C_{\text{peak}}}\right)} \tag{65}$$

In the device shown above, $y_{\text{peak}} = 0\ \mu m, depth = -0.007\ \mu m, C_{\text{peak}} = 5e19\ cm^{-3}, C_{\text{at depth}} = 1e14\ cm^{-3}$. $x_0 = -0.0075\ \mu m$, and $stdDev_x = 0.5 \cdot stdDev_y$.

This doping strategy is used in all later mentioned models and in 3-dimensional cases, the doping profile does not depend on the direction perpendicular to the page. The doping at the drain-end is symmetrical with that in the source-end.

With this modification, the device's conduction band energy along the channel and 0.1nm below the gate oxide-silicon interface now is as shown in Figure 16 below.

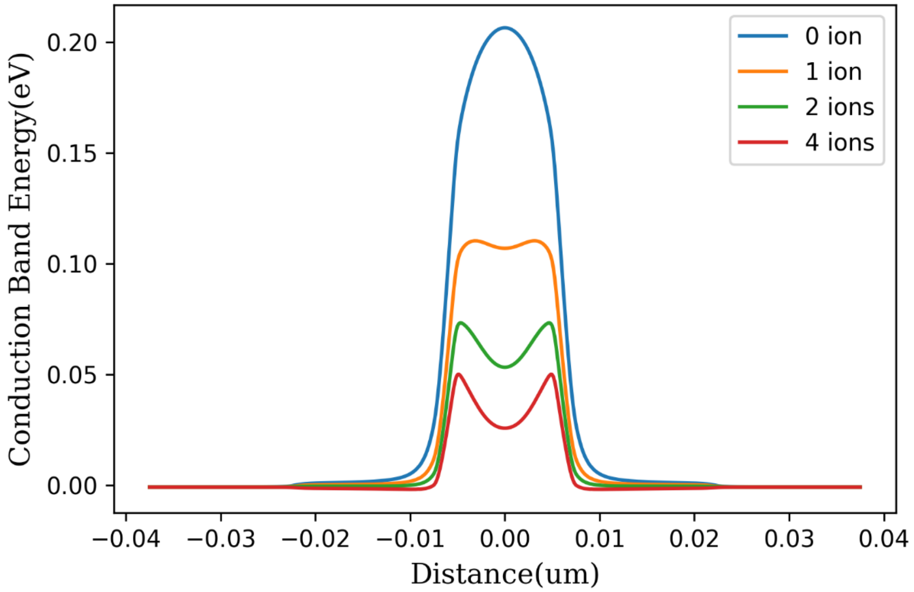

Figure 16. Conduction band energy at zero source drain bias along the channel in 2D exploratory device with Gaussian doping on source and drain.

It is quite clear judging from the figure that Gaussian doping is necessary to remove the numerical errors caused from abrupt doping changes.

It should also be noted that the Gaussian doping profile is what is possible technologically and this is adopted in the following simulations.

3D Exploratory Device Simulation: MOSFET and FinFET

As the next step of the exploratory study to determine the overall behavior of this novel device, two standard 3D FET geometries were modeled to determine the sensitivity to the presence of ions.

The first geometry modeled was the planar n-channel metal–oxide–semiconductor field-effect transistor (MOSFET). For this MOSFET, the gate is on top of the planar oxide layer on top of the device. The source and drain were modeled with a Gaussian doping profile mentioned above.

The second geometry modeled was a Fin Field-Effect Transistor (FinFET) which demonstrates enhanced gate sensitivity [18]. The FinFET geometry causes the electric field in the gate to be more focused around the channel, increasing sensitivity of drain current with gate potential. The geometry and silicon doping were set to match that of the MOSFET. The 3D gate geometry is constructed by attaching a substrate of height 20nm below the channel and the source/drain region. The gate has a total length of 75 nm (nominal channel length of 15 nm and nominal source/drain length of 30 nm with gaussian doping as described earlier) and a cross-section of 5 nm × 5 nm, between two SiO2 slabs.

The detailed 3D geometries for the above discussed MOSFET and FinFET are as shown in Figure 17 below and specific dimensions are shown in Table 1. Again, the light blue region on the top represents electrolyte modeled as insulator, the dark red region represents SiO2, and the lower section represents silicon (red being n-doped, blue being p-doped). Notice that the middle region representing the bilipid membrane is hidden to better show the nanopore and FET structure.

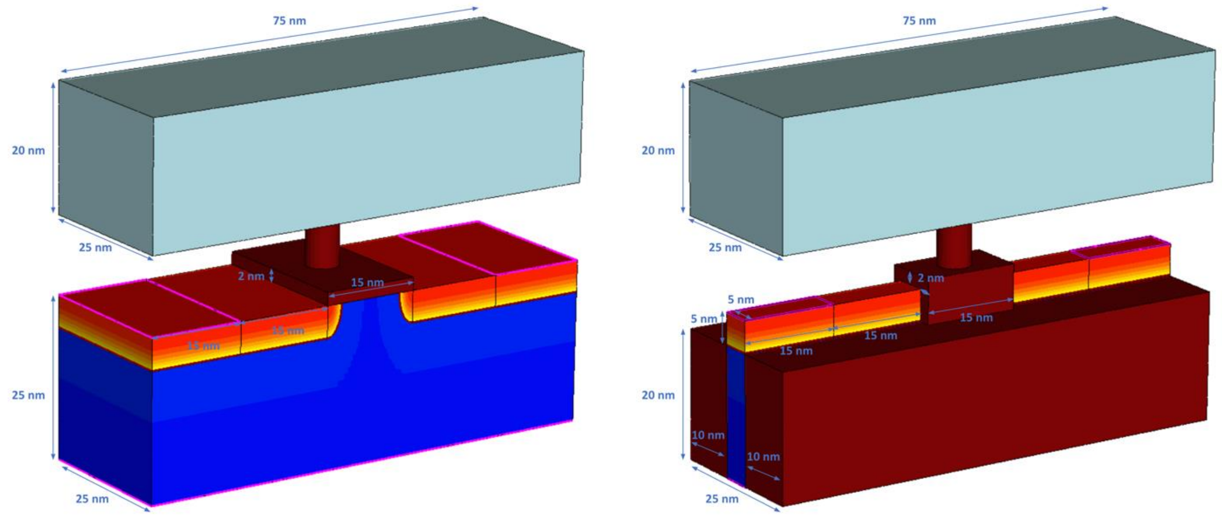

Figure 17. All dimensions used for the 3D model, with the MOSFET topology depicted on the left and FinFET topology depicted on the right. Note that the middle region representing the bilipid membrane is hidden to better show the nanopore and FET structure.

	3D MOSFET	3D FinFET
Source/Drain Width	30 nm (nominal)	30 nm (nominal)
Source/Drain Depth	7 nm (nominal)	7 nm (nominal)
Source/Drain Doping	5e19 cm^{-3} Arsenic	5e19 cm^{-3} Arsenic
Bulk Doping	1e17 cm^{-3} Boron	1e17 cm^{-3} Boron
Nanopore Dimension	10nm (height), 2nm (inner radius), 2.6nm (outer radius), filled with dielectric electrolyte	10nm (height), 2nm (inner radius), 2.6nm (outer radius), filled with dielectric electrolyte
Relative Dielectric Constant of the electrolyte Reservoir	78	78
Relative Dielectric Constant of the Material Between the Water Reservoir and the Device	3[16]	3[16]

Table 1. Simulated FET device dimensions and doping concentrations for exploratory ion sensitivity study.

Both structures were explored by varying the total charge in the nanopore from 0 to 4 ions (charges), which corresponds to a concentration range of 0-52 mM over the whole nanopore volume.

To compare the sensitivity between the two topologies the conduction band energy barrier size was compared. Note that device sensitivity requires comparing the relative change in barrier height from the zero-ion case, which directly relates to the change in drain-source current that could be measured experimentally.

The exploratory studies with ions (charges) placed at the bottom the nanopore clearly indicate that the FinFET geometry has higher sensitivity, as shown in the conduction band plots in Figure 18. This design was tested for 0-4 ions present, with resulting conduction band plotted for each of these cases. While the overall conduction band plot is nearly equivalent for the 4-ion case, the difference in conduction band energy from the case without ions presence is substantially higher. The ratio of these barriers is about 25% higher for the FinFET topology, indicating that the Fin geometry had a significant effect on gating induced by the ions. Based on this result it is clear that the FinFET topology is more sensitive to ions and this device topology was used for all following cases.

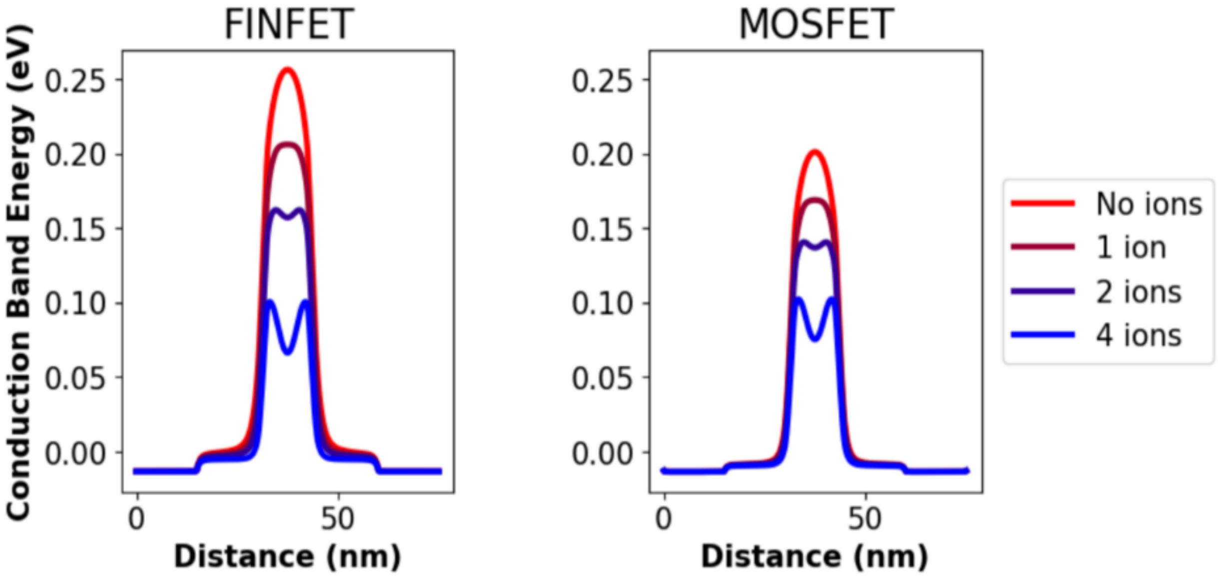

Figure 18. A comparison of the conduction bands of the MOSFET and FinFET geometries varying the ion count in the nanopore from the 3D model. The cutline is along the channel at the center of the device and 0.1nm below the gate oxide-silicon interface.

Chapter 6: Full Electrical Double Layer Device TCAD Simulation

As we established that the FinFET Geometry of the sensor device has a higher sensitivity as discussed in chapter 5, we now proceed to model the full electrical double layer device with the electrolyte solution (for convenience, the electrolyte was taken to be binary symmetric $NaCl$).

The ion concentration in the electrolyte was modeled as a semiconductor with the same intrinsic charge carrier concentration and the surface charge of the DNA and silicon oxide surface were modeled based on the solvent interaction calculated through site-binding model discussed in chapter 3. This meant that the gate potential of the FET is controlled by distribution of ions on the negatively charged nanopore and oxide surface.

The relative dielectric constant of the bilipid membrane is still taken to be 3 based on experimental results [16]. This setup is shown in Figure 19.

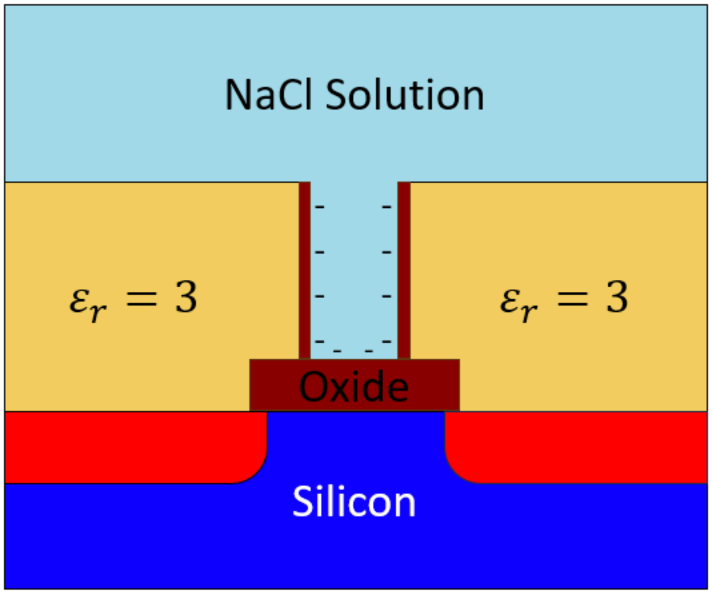

Figure 19. Illustration of the simplified exploratory device, modeling the electrolyte as a semiconductor.

3D Full Electric Double Layer FinFET Sensor Simulation

Taking the full electric double layer setup and reusing the same 3D FinFET geometry and doping from chapter 5, we have the full electric double layer simulation as shown in Figure 20. The light blue region represents the electrolyte reservoir modeled as semiconductor, and the dark red cylinder in the middle represents the DNA nanopore, and the bottom section is the FinFET device. The dielectric lipid membrane around the nanopore is hidden here to better show the nanopore structure.

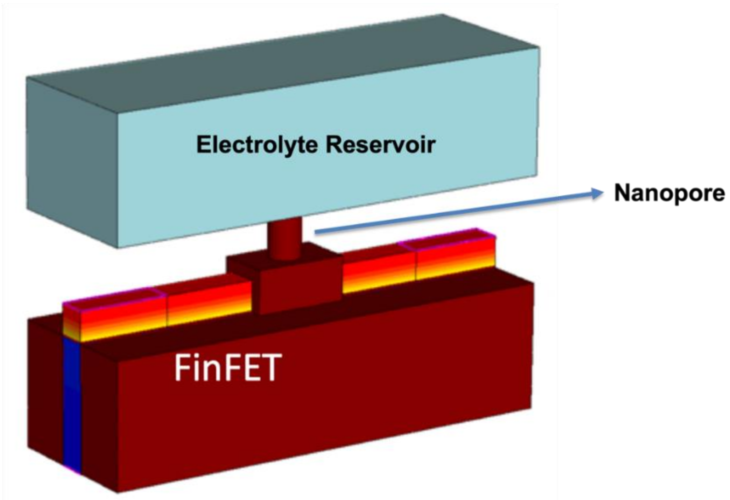

Figure 20. Full electric double layer FinFET device geometry. Note that the lipid membrane is hidden to better show the DNA-nanopore and the FinFET structure.

The simulation results for the geometry is shown in Figure 21. With a grounded substrate and floating electrolyte reservoir, the current through the FinFET with a source drain voltage scanned from 0 to 0.5 V under different ion concentrations was studied.

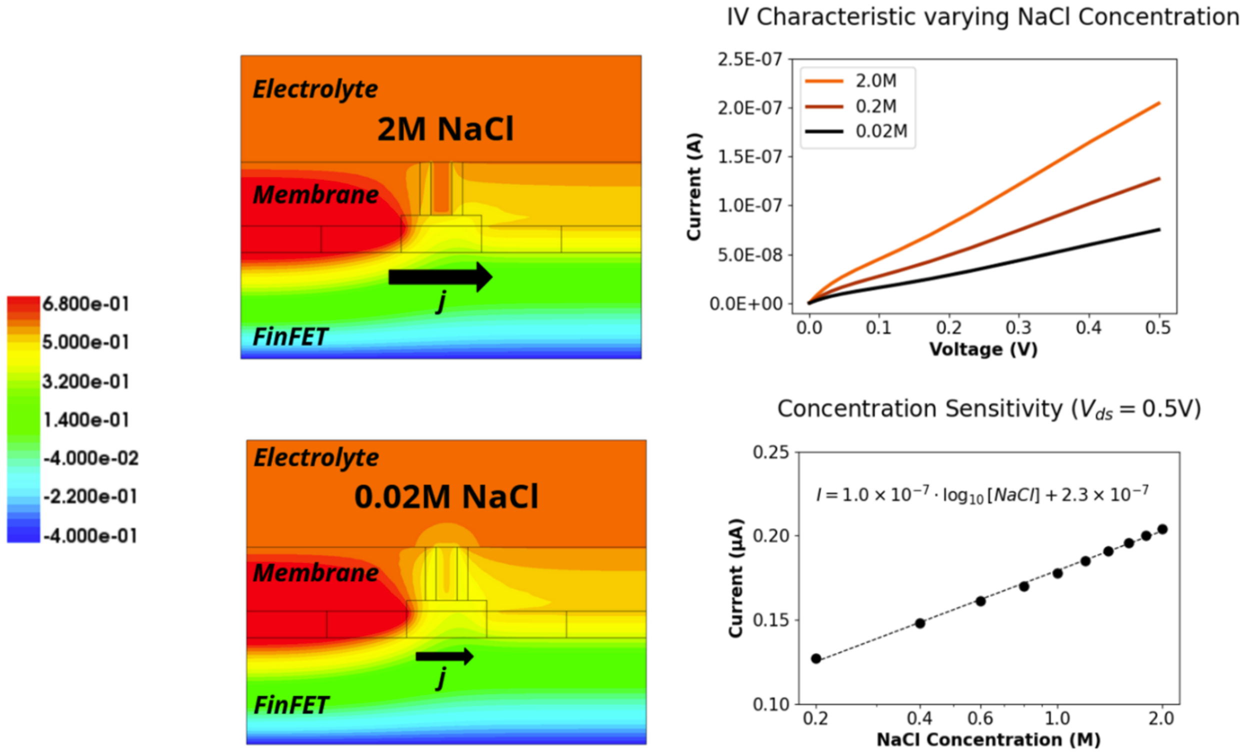

Figure 21. Full electric double layer FinFET device characteristic showing a high sensitivity to ions that follows a logarithmic relationship with ion concentration. The calibration curve formula is shown as an inset on the bottom right plot, with units of molar for the concentration and amperes for the current. The color bar shows the electrostatic potential distribution in Volts.

The current through the FET are within a measurable range, ranging from around 70 nA for 0.02 molar NaCl, which equates to approximately 1 ion in the DNA-nanopore, to 0.2 μA for 2 molar NaCl, which equates to approximately 150 ions in the DNA-nanopore. This indicates that the nanopore ion detection mechanism is feasible and could potentially achieve single ion detection.

In addition, we see a logarithmic relationship between ion concentration and drain current, meaning that with a constant applied bias (0.5V), there is a linear change in current for each order of magnitude change in concentration, indicating a better sensitivity over lower electrolyte concentration. A calibration curve has been constructed using a linear regression ($R^2 > 0.999$) and the formula is given as an inset to the sensitivity plot in Figure 21.

The Effect of Gap Between the DNA-Nanopore and the FET

In all above setups for the proposed DNA-nanopore based sensor studied in this thesis, the nanopore was positioned to be in direct contact with the FET surface, with the charged surface of the silicon oxide creating a circular interface at the bottom of the nanopore. However, it is still possible that there would be a gap between the DNA-nanopore and the gate oxide surface, which would influence the sensor's performance.

In this setup to study the "gap effect", we included a small gap between the nanopore edge and FET surface filled by the modeled electrolyte solution. To test the effect of the nanopore alignment on the induced gate potential, two different spacings were tested as shown in Figure 22 (no gap and 2 nm gap respectively). The spacing of the nanopore and oxide surface was shown to drastically impact the electric potential on the gate, indicating that minimizing the nanopore-oxide gap is necessary for a sensitive device.

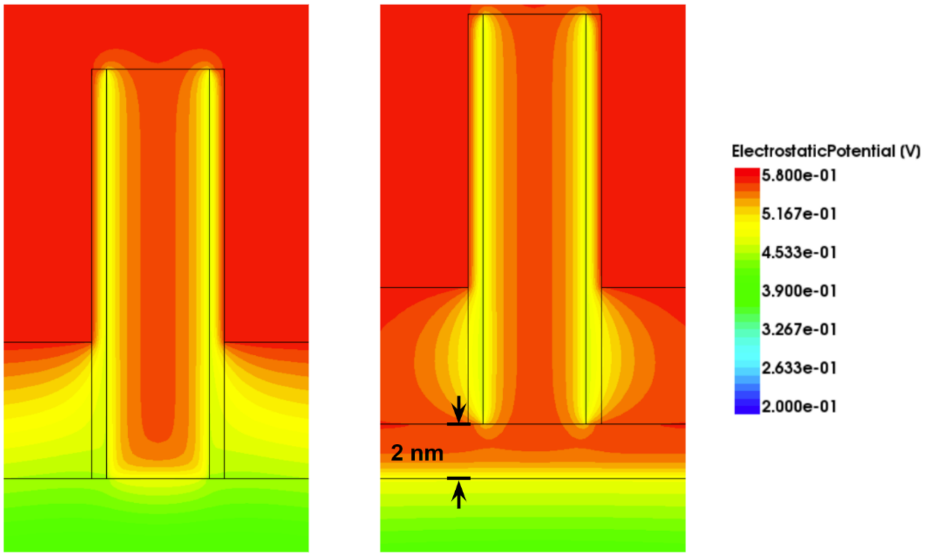

Figure *22*. The effect of nanopore spacing on induced gate potential (3D model). The spacing of 2nm corresponds to the Debye length of the system, showing that a low gap is crucial for ion sensing.

Chapter 7: Conclusion and Future Work

Conclusion of Main Findings

Our results show that single ion detection is possible in the proposed electrical double layer based DNA-origami nanopore/FET device, with increased sensitivity using the FinFET topology over a standard MOSFET design.

The surface charge of the DNA nanopore and the gate oxide creates an overlapping electrical double layer that acts as a gate to the FET. This effect was demonstrated both in the 3D drift-diffusion TCAD solver and in the 1D Poisson-Boltzmann numerical solvers. Using this comparison, we were able to demonstrate that the 3D TCAD results are grounded in the electrical double layer theory. When the 3D model was used to model ion distribution in the full device, the proposed topology shows high sensitivity to ion concentration change and has promise as a direct probe across a biotic interface.

Additional levels of theory were studied to improve the accuracy of the model by accounting for finite ion size and polarization of the electrolyte. While this work did not directly compare to experiment, the modified Poisson-Boltzmann equation used to analyze the electrical double layer behavior were developed based on experimental results. The finite ion size model was developed to address unrealistically high concentrations predicted near the interface and has been validated directly with experimental nanoconfined systems [19]. In addition, the electric field dependent permittivity model has been shown to be effective in nanoconfined spaces, accurately reproducing the measured potential from experiment [11]. These modifications of the electrical double layer model have noticeable but limited impact on the electrolyte properties, as the overall effect on the electrostatic potential was small as shown in Figure 10, proving that the simpler model used by the 3D TCAD simulations provides a reasonable estimate of nanopore ion interactions in the nanopores considered.

Limitations and Future Works

Our simulation and results were limited to static (steady state) ion concentrations. In this sense, we do not study the transient effect and thus do not know how fast the electrical double layer would form and cause a change in the FET current.

Our results were also limited to a simple binary electrolyte. In a real biological system, there would be many kinds of ions and organic molecules present, which may impact the sensitivity of the device.

Additionally, the TCAD model used for full 3D device geometries did not consider the two modifications (finite ion size effect and electric field dependent permittivity) studied in 1D. To be specific, in 3D TCAD models, cations and anions in electrolyte are still considered point charges and the electrolyte has a constant permittivity. Although we only see a small difference in electrostatic potential with the modification added in the slab case comparison as shown in Figure 10, it would be good to incorporate these modifications into future 3D models.

This study was also limited in the sense that the DNA-origami nanopore and the lipid bilayer membrane are both modeled as isotropic dielectric materials. The DNA nanopore is modeled as silicon oxide and the lipid bilayer membrane has a relative permittivity of 3 taking from experimental measurements [16]. However, for example, it is well-known that the lipid bilayer of the cellular membrane has hydrophilic and hydrophobic layers each with different dielectric properties as shown in Figure 23. Future works can build on this model to look at a more complex model of the lipid bilayer membrane to include any effects that may cause more complex electrical interactions.

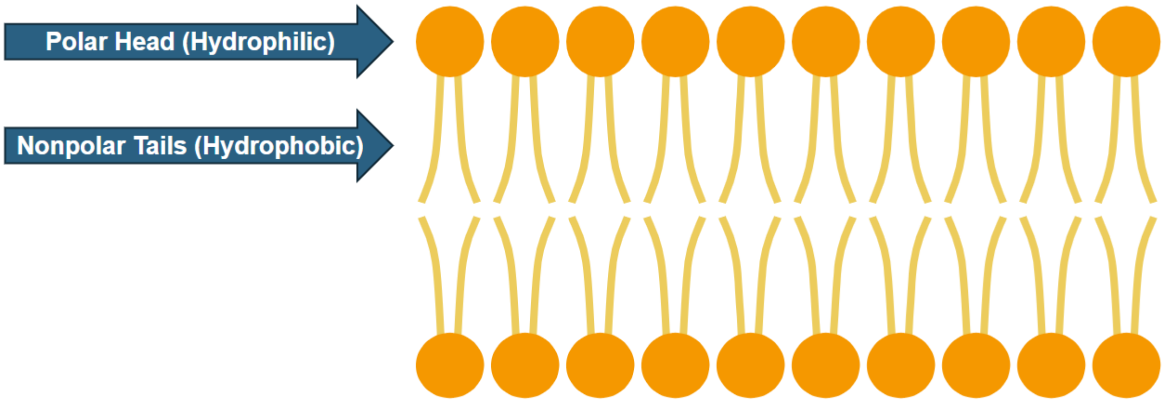

Figure 23. A simplified illustration of the lipid bilayer membrane.

It is also worth noting that although in this work the DNA-nanopore is modeled as a perfect cylinder, in reality, the shape is closer to a six helix bundle. Additional atomic level modeling tools like molecular dynamics (MD) could also be applied to study the DNA-nanopore structure, and our collaborator has showed in MD simulations that the DNA-nanopore bundle could deviate from cylindrical structure as strands spread apart away from the lipid bilayer membrane [6], as shown in Figure 24. The reason behind such phenomena and its implications on the device function should be further studied.

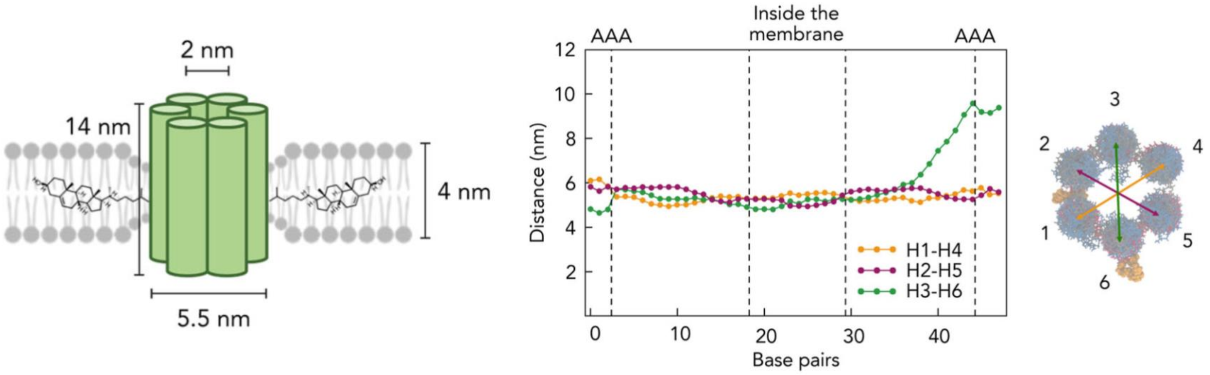

Figure 24. Molecular dynamics simulation result from our collaborator taken from [6]. The right plot shows the average distance between opposing strands. We can see strands 3 and 6 become further apart on one side and thus make the DNA-nanopore deviates from a cylindrical shape.

Additionally, as this is a complex interface, future work could look at the interaction of the DNA nanopore with the membrane, potentially including ion leakage caused by the interface. Similarly, the leakage effect on the gate-nanopore interface is also not rigorously studied and needs more attention. The potential leakage locations proposed are shown in Figure 25.

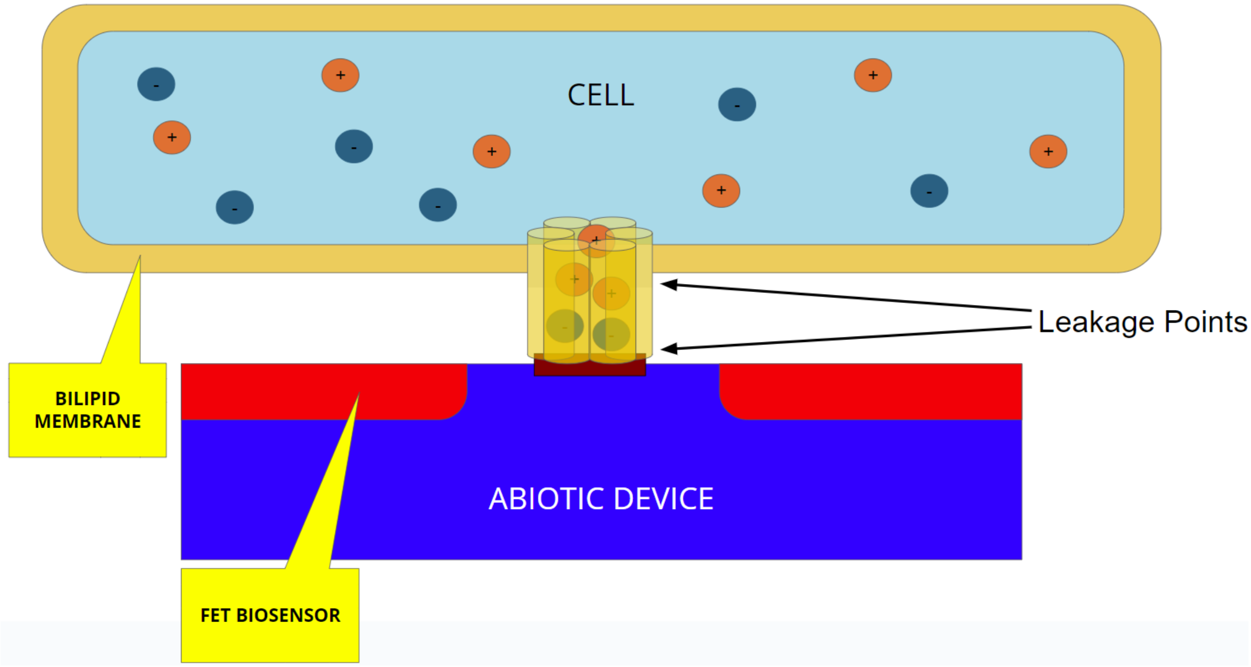

Figure 25. Potential leakage points in proposed DNA-nanopore FET device.

In all, this work can provide a starting point for future explorations of more complex nanopore sensors, especially in the context of bridging semiconductor devices with biological systems.

References

[1] Fattahi P, Yang G, Kim G and Abidian M R 2014 A review of organic and inorganic biomaterials for neural interfaces *Adv. Mater. Deerfield Beach Fla* **26** 1846–85

[2] Obien M E J, Deligkaris K, Bullmann T, Bakkum D J and Frey U 2014 Revealing neuronal function through microelectrode array recordings *Front. Neurosci.* **8** 423

[3] Abbott J, Ye T, Qin L, Jorgolli M, Gertner R S, Ham D and Park H 2017 CMOS nanoelectrode array for all-electrical intracellular electrophysiological imaging *Nat. Nanotechnol.* **12** 460–6

[4] Spira M E, Shmoel N, Huang S-H M and Erez H 2018 Multisite Attenuated Intracellular Recordings by Extracellular Multielectrode Arrays, a Perspective *Front. Neurosci.* **12**

[5] Burns J R, Stulz E and Howorka S 2013 Self-Assembled DNA Nanopores That Span Lipid Bilayers *Nano Lett.* **13** 2351–6

[6] Luo L, Manda S, Park Y, Demir B, Sanchez J, Anantram M P, Oren E E, Gopinath A and Rolandi M 2023 DNA nanopores as artificial membrane channels for bioprotonics *Nat. Commun.* **14** 5364

[7] Livernois W, Cao P (Simon), Saha S, Ding Q, Gopinath A and Anantram M P 2024 Ion detection in a DNA nanopore FET device *Nanotechnology* **35** 325202

[8] Roozbahani G M, Chen X, Zhang Y, Wang L and Guan X 2020 Nanopore detection of metal ions: Current status and future directions *Small Methods* **4** 2000266

[9] Bikerman J J 1942 XXXIX. Structure and capacity of electrical double layer *Lond. Edinb. Dublin Philos. Mag. J. Sci.* **33** 384–97

[10] Horng T-L, Tsai P-H and Lin T-C 2017 Modification of Bikerman model with specific ion sizes *Comput. Math. Biophys.* **5** 142–9

[11] Das S, Chakraborty S and Mitra S K 2012 Redefining electrical double layer thickness in narrow confinements: Effect of solvent polarization *Phys. Rev. E* **85** 051508

[12] Gray C G and Stiles P J 2018 Nonlinear electrostatics: the Poisson-Boltzmann equation *Eur. J. Phys.* **39** 1–27

[13] Yates D E, Levine S and Healy T W 1974 Site-binding model of the electrical double layer at the oxide/water interface *J. Chem. Soc. Faraday Trans. 1 Phys. Chem. Condens. Phases* **70** 1807–18

[14] Bandiziol A, Palestri P, Pittino F, Esseni D and Selmi L 2015 A TCAD-Based Methodology to Model the Site-Binding Charge at ISFET/Electrolyte Interfaces *IEEE Trans. Electron Devices* **62** 3379–86

[15] Pittino F, Palestri P, Scarbolo P, Esseni D and Selmi L 2014 Models for the use of commercial TCAD in the analysis of silicon-based integrated biosensors *Solid-State Electron.* **98** 63–9

[16] Gramse G, Dols-Perez A, Edwards M A, Fumagalli L and Gomila G 2013 Nanoscale measurement of the dielectric constant of supported lipid bilayers in aqueous solutions with electrostatic force microscopy *Biophys. J.* **104** 1257–62

[17] Dennard R H, Gaensslen Fritz H, Yu H-N, Leo Rideovt V, Bassous E and Leblanc A R 2007 Design of ion-implanted MOSFET's with very small physical dimensions *IEEE Solid-State Circuits Soc. Newsl.* **12** 38–50
[18] Wu Y-C and Jhan Y-R 2018 3D FinFET with Lg = 15 nm and Lg = 10 nm Simulation *3D TCAD Simulation for CMOS Nanoeletronic Devices* ed Y-C Wu and Y-R Jhan (Singapore: Springer) pp 91–183
[19] Pardon G and van der Wijngaart W 2013 Modeling and simulation of electrostatically gated nanochannels *Adv. Colloid Interface Sci.* **199–200** 78–94

Appendix

Code for 1D Models of EDL

Following are the code files used to solve the 4 EDL models (original Poisson-Boltzmann, finite ion size, electric field dependent permittivity, modified Poisson-Boltzmann).

```
close all; clear; clc;

%% constants and conditions
q = 1.6e-19; % charge columb C
kB = 1.38e-23; % boltzman J/K
T = 300; % temp K
ep_r = 79.8; % relative permitivity of 0.5M NaCl solution Unitless
c_b = 0.2*6.022e26; % bulk concentration fo NaCl solution (0.2M) Unitless
ep = 8.854e-12; % permittivity of free space F/m
beta = 1/(kB*T); % inverse thermal energy 1/J
a = 0.5e-9; % radius m
phi0 = 2*c_b*a*a*a; % cubic m

prefactor = 2*q*c_b/(ep*ep_r);
factor_in_sinh = beta*q;

sigma = 1.4e18; %electrons/m^2
zeta_potential = asinh(-q*sigma/sqrt(8*ep*ep_r*c_b*kB*T))*2*kB*T/q;

mu_p = 6.14e-30; %  C*m
n = 1.33; % refractive index of water

%% Init Setups
m = 1000; h=5e-9/m; N=m-1;% m segments, m+1 points, N*N jac matrix
x=0:h:5e-9;  x=x'; % unit: m

uc = zeta_potential.*exp(-x./(3e-10));  % initial guess, exponential potential

u1=uc(2:m);  % Take off two boundary conditions

e = ones(N,1); F=e;     % initial set-up for F(i)


%% begin iterations of PB Newton's method:
tol = 1.e-8; err = 10.0; % initial set-up for tolerance and error
k = 0; kmax=1000; % k: itr #
while err > tol && k < kmax

  for i=1:N
     jac(i,i)=(-2-h^2*prefactor*factor_in_sinh*cosh(factor_in_sinh*u1(i)))/h^2;  %
Jacobian diagonals.

     F(i) = (uc(i)-2*uc(i+1)+uc(i+2))/h^2 -
(prefactor*sinh(factor_in_sinh*uc(i+1))); % F(i)
```

```
  end

  for i=1:N-1
   jac(i,i+1) = 1/h^2; jac(i+1,i)=1/h^2; % Jacobian off diagonals.
  end

  delta = -jac\F;
  u2 = u1 + delta; % Compute new psi k
  k = k + 1;
  err = max(abs(u2-u1));
  u1 = u2;
  uc=[zeta_potential
      u2
      -1e-8]; % Keeping boundary conditions

end

uc_PB = uc;

plot(x,uc_PB)
hold on
axis([0 1e-9 -0.12 0])
xlabel("distance to electrode (m)");
ylabel("potential (V)");

Legend=cell(5,1);
Legend{1}='PB';


%% begin iterations of Finite-ion size Newton's method:
tol = 1.e-8; err = 10.0; % initial set-up for tolerance and error
k = 0; kmax=1000; % k: itr #
while err > tol && k < kmax

  for i=1:N
     % Jacobian diagonals.
     jac(i,i)=(-2-h^2*prefactor*factor_in_sinh*(-
phi0*sinh(factor_in_sinh*u1(i))^2+phi0*cosh(factor_in_sinh*u1(i))^2-(phi0-
1)*cosh(factor_in_sinh*u1(i)))/(phi0*cosh(factor_in_sinh*u1(i))-phi0+1)^2)/h^2;
     % F(i)
     F(i) = (uc(i)-2*uc(i+1)+uc(i+2))/h^2 -
(prefactor*sinh(factor_in_sinh*uc(i+1))/(1-phi0+phi0*cosh(factor_in_sinh*uc(i+1))));
  end

  for i=1:N-1
   jac(i,i+1) = 1/h^2; jac(i+1,i)=1/h^2; % Jacobian off diagonals.
  end

  delta = -jac\F;
  u2 = u1 + delta; % Compute new psi k
  k = k + 1;
  err = max(abs(u2-u1));
  u1 = u2;
  uc=[zeta_potential
```

```
      u2
      -1e-8]; % Keeping boundary conditions

end

uc_finite_ion = uc;

plot(x,uc_finite_ion)
hold on
axis([0 1e-9 -0.12 0])
xlabel("distance to electrode (m)");
ylabel("potential (V)");
Legend{2}='Finite Ion Size - PB';

%% begin iterations of Booth-PB Newton's method:

ep_itr = ones(m+1,1)*ep_r;

tol = 1.e-8; err = 10.0; % initial set-up for tolerance and error
k = 0; kmax=1000; % k: itr #
while err > tol && k < kmax

  prefactor = 2*q*c_b/ep;

  for i=1:N
     jac(i,i)=(-2*ep_itr(i+1)-h*(ep_itr(i+2)-ep_itr(i+1))/h-
h^2*prefactor*factor_in_sinh*cosh(factor_in_sinh*u1(i)))/h^2;  % Jacobian diagonals.

     F(i) = (uc(i)-2*uc(i+1)+uc(i+2))/h^2*ep_itr(i+1) + (ep_itr(i+2)-ep_itr(i+1))/h *
(uc(i+2)-uc(i+1))/h -(prefactor*sinh(factor_in_sinh*uc(i+1))); % F(i)

  end

  for i=1:N-1
   jac(i,i+1) = 1/h^2*ep_itr(i+1) + 1/h*(ep_itr(i+2)-ep_itr(i+1))/h;
   jac(i+1,i)=1/h^2*ep_itr(i+1); % Jacobian off diagonals.
  end

  delta = -jac\F;
  u2 = u1 + delta; % Compute new psi k
  k = k + 1;
  err = max(abs(u2-u1));
  u1 = u2;
  uc=[zeta_potential
      u2
      -1e-8]; % Keeping boundary conditions

  for i=1:m
      E = abs(-(uc(i+1)-uc(i))/h);
      beta_booth = 5*mu_p*(n^2 + 2)/(2*kB*T);
      updated_itr = n^2+(ep_r-n^2)*(3/(beta_booth*E))*(coth(beta_booth*E)-
1/(beta_booth*E));
      % err = max(abs(updated_itr-ep_itr(i)),err);
      ep_itr(i) = updated_itr; % update ep here
  end
```

```
end

uc_Booth = uc;

plot(x,uc_Booth)
hold on
axis([0 1e-9 -0.12 0])
xlabel("distance to electrode (m)");
ylabel("potential (V)");

Legend{3}='Booth - PB';


%% begin iterations of MPB Newton's method:
tol = 1.e-8; err = 10.0; % initial set-up for tolerance and error
k = 0; kmax=1000; % k: itr #

ep_itr = ones(m+1,1)*ep_r;

while err > tol && k < kmax

  prefactor = 2*q*c_b/ep;

  for i=1:N
     % Jacobian diagonals.
     jac(i,i)=(-2*ep_itr(i+1)-h*(ep_itr(i+2)-ep_itr(i+1))/h-
h^2*prefactor*factor_in_sinh*(-
phi0*sinh(factor_in_sinh*u1(i))^2+phi0*cosh(factor_in_sinh*u1(i))^2-(phi0-
1)*cosh(factor_in_sinh*u1(i)))/(phi0*cosh(factor_in_sinh*u1(i))-phi0+1)^2)/h^2;
     % F(i)
     F(i) = (uc(i)-2*uc(i+1)+uc(i+2))/h^2*ep_itr(i+1) + (ep_itr(i+2)-ep_itr(i+1))/h *
(uc(i+2)-uc(i+1))/h  -(prefactor*sinh(factor_in_sinh*uc(i+1))/(1-
phi0+phi0*cosh(factor_in_sinh*uc(i+1))));
  end

  for i=1:N-1
   jac(i,i+1) = 1/h^2*ep_itr(i+1) + 1/h*(ep_itr(i+2)-ep_itr(i+1))/h;
   jac(i+1,i)=1/h^2*ep_itr(i+1); % Jacobian off diagonals.
  end

  delta = -jac\F;
  u2 = u1 + delta; % Compute new psi k
  k = k + 1;
  err = max(abs(u2-u1));
  u1 = u2;
  uc=[zeta_potential
      u2
      -1e-8]; % Keeping boundary conditions

  for i=1:m
      E = abs(-(uc(i+1)-uc(i))/h);
      beta_booth = 5*mu_p*(n^2 + 2)/(2*kB*T);
      ep_itr(i) = n^2+(ep_r-n^2)*(3/(beta_booth*E))*(coth(beta_booth*E)-
1/(beta_booth*E)); % update ep here
```

```
  end

end

uc_MPB = uc;

plot(x,uc_MPB)
hold on
axis([0 1e-9 -0.12 0])
xlabel("distance to electrode (m)");
ylabel("potential (V)");
Legend{4}='MPB';

%% Calculate E field from Potential

hold on

E = ones(m+1,1);

for i=1:m
      E(i) = abs(-(uc(i)-uc(i+1))/h);
end

E(end) = E(end-1);

plot(E,ep_itr)

%% Plot E field permittivity relation

h_E= 5e8/m;
E = 0:h_E:5e8;

beta_booth = 5*mu_p*(n^2 + 2)/(2*kB*T);
ep_E = n.^2+(ep_r-n.^2).*(3./(beta_booth.*E)).*(coth(beta_booth.*E)-
1./(beta_booth.*E));

plot(E,ep_E,LineWidth=2)

fontsize(gcf,scale=1.5)
xlabel("Electric Field (V/m)");
ylabel("Relative Permittivity of Water");

%% Plotting, compare Analytical Sol to PB

close all;
hold on

Legend=cell(2,1);

plot(x,uc_PB,"bo")
Legend{1}='Poisson-Boltzmann Equation Numerical Solution';

alpha = tanh(beta*q*zeta_potential/4);
l_d =sqrt(ep_r*ep*kB*T/(2*q^2*c_b));
kappa = 1/l_d;
```

```
h= 5e-9/m;
x = 0:h:5e-9;
phi = 2*kB*T/q*log((1+alpha*exp(-kappa*x))./(1-alpha*exp(-kappa*x)));

plot(x,phi,'r-',LineWidth=2)
hold on
xlabel("Distance to charged surface (m)");
ylabel("Potential (V)");
Legend{2}='Poisson-Boltzmann Equation Analytical Solution';

legend(Legend,'Location','southeast')
axis([0 1e-9 -0.12 0])

%% Plotting, all

close all;

plot(x,uc_PB,LineWidth=2)
hold on
xlabel("distance to electrode (m)");
ylabel("potential (V)");

Legend=cell(4,1);
Legend{1}='Original Poisson-Boltzmann Equation';

plot(x,uc_finite_ion,LineWidth=2)
hold on
xlabel("distance to electrode (m)");
ylabel("potential (V)");
Legend{2}='Finite Ion Size Effect';

plot(x,uc_Booth,LineWidth=2)
hold on
xlabel("distance to electrode (m)");
ylabel("potential (V)");
Legend{3}='Electric Field Dependent Permittivity';

plot(x,uc_MPB,LineWidth=2)
hold on
xlabel("Distance to charged surface (m)");
ylabel("Potential (V)");
Legend{4}='Modified Poisson-Boltzmann Equation';

% plot(x,phi)
% hold on
% xlabel("distance to electrode (m)");
% ylabel("potential (V)");
% Legend{5}='PB - Analytical Sol';

%title('Solution for PB (Wall Geometry)')
legend(Legend,'Location','southeast')
% axis([0 1e-9 -0.12 0])
xlim([0 1e-9]);
```

```
%% Ploting, PB & MPB

close all;

plot(x,uc_PB,LineWidth=2)
hold on
plot(x,uc_MPB,LineWidth=2)
xlabel("Distance to Charged Surface (m)");
ylabel("Potential (V)");

Legend=cell(2,1);
Legend{1}='Original Poisson-Boltzmann Equation;
Legend{2}='Modified Poisson-Boltzmann Equation;

title('Solution for 1D PB and Modified-PB for Wall Geometry')
legend(Legend) %, 'Location','southeast'
% axis([0 1e-9 -0.12 0])
xlim([0 1e-9]);
fontsize(gcf,scale=1.5)
```

Code for SiO2 Charge Calculation

Following are the code files used to calculate the surface charge concentration of SiO2 in electrolyte using site-binding model, solved self-consistently with Grahame equation.

```
close all; clear; clc;

%% Plot

pHs = 0:0.1:14;
sigmas_e_per_area = arrayfun(@get_sigma, pHs);
plot(pHs,sigmas_e_per_area,LineWidth=2)

xlabel("pH");
ylabel("SiO2 surface charge (q/cm^2)");
ylim([-6e14, 1e14])

%% Calculate sigma from pH Function

function sigma_e_per_area = get_sigma(pH)

% constants and conditions
q = 1.6e-19; % charge columb C
kB = 1.38e-23; % boltzman J/K
T = 300; % temp K
ep_r = 79.8; % relative permitivity of NaCl solution Unitless
H_b_M = 10^(-pH); % bulk concentration fo H+ solution, M
C_NaCl = 0.2; % NaCl concentration in M
H_b = C_NaCl*6.022e23*1000; % bulk concentration fo H+ solution m^-3
ep = 8.854e-12; % permittivity of free space F/m
beta = 1/(kB*T); % inverse thermal energy 1/J
Nsil = 5e14*1e4; % m^-3
Ka = 1e-6; % unitless
```

```
Kb = 1e2; % unitless

zeta = 0;  % initial guess, zeta potential = 0V
tol = 1.e-8; err = 10.0; % initial set-up for tolerance and error

% begin iterations:
k = 1; kmax=1000; % k: itr #
zetas = zeros(1,kmax);
while err > tol && k < kmax

    H_s_M = H_b_M*exp(-q*zeta/(kB*T));
    sigma = q*Nsil*(H_s_M^2-Ka*Kb)/(H_s_M^2+Kb*H_s_M+Ka*Kb);

    zeta0 = 2*kB*T/q*asinh(sigma/sqrt(8*ep_r*ep*H_b*kB*T));

  k = k + 1;
  err = abs(zeta0-zeta);
  zeta = zeta0*0.5+zeta*0.5;
  zetas(k) = zeta;

end

sigma_e_per_area = sigma/q*1e-4;
end
```